

An overview of desorption parameters of Volatile and Complex Organic Molecules

A systematic dig on experimental literature

N.F.W. Ligterink¹ & M. Minissale²

¹ Space Research & Planetary Sciences, University of Bern, Switzerland
 e-mail: niels.ligterink@unibe.ch

² Aix Marseille Univ, CNRS, PIIM, Marseille, France
 e-mail: marco.minissale@univ-amu.fr

Received March 16, 2023; accepted June 15, 2023

ABSTRACT

Context. Many molecules observed in the interstellar medium are thought to result from thermal desorption of ices. Parameters such as desorption energy and pre-exponential frequency factor are essential to describe the desorption of molecules. Experimental determinations of these parameters are missing for many molecules, including those found in the interstellar medium.

Aims. The objective of this work is to expand the number of molecules for which desorption parameters are available, by collecting and re-analysing experimental temperature programmed desorption data that are present in the literature.

Methods. Transition State Theory (TST) is used in combination with the Redhead equation to determine desorption parameters. Experimental data and molecular constants (e.g., mass, moment of inertia) are collected and given as input.

Results. Using the Redhead-TST method, the desorption parameters for 133 molecules have been determined. The Redhead-TST method is found to provide reliable results that agree well with desorption parameters determined with more rigorous experimental methods. The importance of using accurately determined pre-exponential frequency factors to simulate desorption profiles is emphasised. The large amount of data allows to look for trends, the most important is the relationship $\log_{10}(\nu) = 2.65\ln(m) + 8.07$, where ν is the pre-exponential frequency factor and m the mass of the molecule.

Conclusions. The data collected in this work allow to model the thermal desorption of molecules and help understand changes in chemical and elemental composition of interstellar environments.

Key words. Desorption - Complex Organic Molecules - Volatile Molecules - Interstellar Medium - Transition State Theory - Redhead equation

1. Introduction

Desorption of molecules from and adsorption of gaseous species on a surface play a pivotal role in regulating physical processes and setting the chemical composition of environments in the interstellar medium (ISM), star- and planet-forming regions, and solar system objects. For example, the chemical composition of hot core and corinos, compact regions of warm and molecule-rich gas surrounding protostars, are largely explained by the desorption of species from ice-coated dust grains (e.g., Ligterink et al. 2018b, 2020, 2021, 2022; Bøgelund et al. 2019; Gorai et al. 2020; Yang et al. 2021; Hsu et al. 2022; Nazari et al. 2022; Bianchi et al. 2022; Zhang et al. 2023). The temperature of interstellar grains and their ice mantles dictates which molecules adsorb and consequently take part in chemical reactions (Jin & Garrod 2020; Garrod et al. 2022). The molecular composition of comets like 67P/Churyumov-Gerasimenko is largely set by which species have remained frozen since its formation or have frozen-out on its surface since (e.g., Mumma & Charnley 2011; Goesmann et al. 2015; Altweig et al. 2016; Rubin et al. 2019). Frozen molecules are found on the surfaces of planets and moons in the solar system, where seasonal changes alter sublimation rates and in turn affect atmospheric processes and chemical composition (Fray & Schmitt 2009), for example on Triton (Bertrand

et al. 2022) or Pluto (Johnson et al. 2021). To interpret observational data and model physical and chemical processes, empirical equations are employed to describe the desorption/adsorption process. For these equations, molecule-specific parameters need to be known.

The theoretical framework and experimental methods for thermal desorption studies are well described in astrophysical and astrochemical literature (see reviews by Burke & Brown 2010; Minissale et al. 2022). In short, to simulate the desorption rate the Polanyi-Wigner equation is generally used:

$$-\frac{dN}{dt} = \nu_n \cdot N^n \cdot \exp\left(\frac{E_{des}}{T}\right), \quad (1)$$

where ν_n the pre-exponential frequency factor with value $\text{molecules}^{1-n} \text{ s}^{-1}$ (also often denoted as A_n and where n is the desorption order with $n = 0, 1, 2$), N the surface coverage in molecules cm^{-2} (also often denoted as θ), $n (= 0, 1, 2)$ the order of desorption, E_{des} the desorption energy in K, and T the temperature of the surface. The order of desorption is given as zeroth, first, or second. Zeroth order desorption is associated with multilayer desorption, while first order desorption with (sub)monolayer desorption. The desorption energy can also be

given in Joule by changing the exponent to $E_{\text{des}} k_{\text{B}}^{-1}$ (k_{B} = Boltzmann constant) or in Joule mol $^{-1}$ by changing the exponent to $E_{\text{des}} R^{-1}$ (R = ideal gas constant). Second order desorption is possible, and is for example observed with processes such as recombinative desorption, where two species react to form the desorbing product. However, as this type of desorption is hardly encountered within the astrochemical literature, second order desorption is ignored in the remainder of this publication.

There are a variety of experimental methods to determine the desorption parameters n , ν , and E_{des} , most of them based on the Temperature Programmed Desorption (TPD) technique or a variation thereof. In a typical TPD experiment, a surface held at low temperature under vacuum conditions is exposed and covered with a given adsorbate. Next, the temperature of the surface is linearly increased. At some point the adsorbate will start desorbing and continues to do so until the adsorbate is fully removed from the surface. The release of adsorbate to the gas-phase can be traced with a variety of instruments, but usually a mass spectrometry technique is employed. The measured desorption trace can be analysed to find the desorption parameters, for example with leading edge, Redhead, heating variation, inversion, or Arrhenius analysis (e.g., King 1975; De Jong & Niemantsverdriet 1990a,b; Tait et al. 2005a).

There are a number of limitation to the experimental determination of desorption parameters, specifically relating to experimental efforts and safety. Currently, the number of molecules detected in the interstellar medium is about 270^{1,2} (McGuire 2022) and more are detected every year. Because experiments are time consuming, it is challenging to keep up with the number of detections and provide desorption parameters for all species. Furthermore, some molecules are difficult to work with, either because they are chemically unstable (e.g., PH₂COOH, CH₃OOH, c-C₃H₄O) or highly toxic (e.g., HCN, CH₃NCO, H₂P(O)OH). To bridge the gap between the availability of experimentally determined desorption parameters and the needs of the community, alternative approaches are needed. Computational techniques such as Machine Learning (Villadsen et al. 2022), Bayesian inference (Heyl et al. 2022), DFT calculations (Ferrero et al. 2022; Piacentino & Öberg 2022), or quantum mechanical methods (Germain et al. 2022; Bovolenta et al. 2022; Tinacci et al. 2022) help fill the gap. However, there also exists a rich experimental literature of TPD experiments that have been used for the identification of molecules produced in experiments that simulate chemical processes in extraterrestrial ice (for brevity named “chemical TPDs”), but not to assess their desorption parameters. Because this type of data is in essence the same as what is used for the determination of desorption parameters, it raises the question if chemical TPD traces can be used to determine pre-exponential factors and desorption energies and in this way contribute more of these essential parameters to the literature.

In this study, chemical TPD traces are collected from laboratory literature and analysed with a combination of Transition State Theory and the Redhead method (Redhead-TST) to determine the pre-factor and desorption energies of 133 molecules. The methods are presented in Sect. 2 and the resulting data in Sect. 3. Implications for astrophysical and astrochemical studies are discussed in Sect. 4.

2. Methods

This work makes use of an analysis method based on the Redhead equation and Transition State Theory, and is indicated as the Redhead-TST method throughout this manuscript. Furthermore, desorption energies and pre-exponential factors are obtained from TPD data that are used for molecule identification. The Redhead-TST method and the data set are introduced in the following sections and a visual summary is presented in Fig. 1.

2.1. Redhead-TST formalism

To determine the desorption energies of molecules from TPD data, the Redhead equation is used (Redhead 1962; King 1975):

$$E_{\text{Redhead}} = T_{\text{peak}} \cdot \left(\ln \left(\frac{\nu_{\text{TST}} T_{\text{peak}}}{\beta} \right) - 3.64 \right) \quad (2)$$

This equation takes the peak of the desorption trace (T_{peak} , K) in combination with the heating rate (β , K s $^{-1}$) and a pre-exponential factor (ν , s $^{-1}$) to determine E_{des} in K energy units. This equation only applies to first order desorption, which generally applies to (sub-)monolayer coverage. It is not used for zeroth order desorption processes, which is usually the case for multi-layer desorption. Redhead (1962) showed that for ν/β values of $10^8 - 10^{13}$ K $^{-1}$, the relation between E_{des} and T_{peak} is nearly linear, within a $\pm 1.5\%$ accuracy. For values of $\nu/\beta > 10^{13}$ K $^{-1}$, we verified that this relationship holds by comparing literature results with those retrieved from the Redhead equation when the same parameters are used (see Sect. 3.2). While the Redhead equation is not the most accurate analysis method to determine desorption energies (De Jong & Niemantsverdriet 1990b,a), the simplicity of this equation makes it very suitable for the analysis of TPD data that have been recorded for other purposes, such as the molecule identification, rather than their desorption parameters. Data of this type can be low in signal to noise ratio or have a poorly defined desorption trace shape, which make other methods, such as the leading edge analysis (De Jong & Niemantsverdriet 1990b,a) less suitable to analyse it with.

The value for ν used in the Redhead equation is usually assumed and taken to be $10^{12} - 10^{13}$ s $^{-1}$. While these values are suitable for small molecules and atoms, they significantly underestimate the pre-exponential factor for larger species with more degrees of freedom. In this work, the pre-exponential factor is therefore calculated by Transition State Theory (TST), following the equation:

$$\nu_{\text{TST}} = \frac{k_{\text{B}} \cdot T_{\text{peak}}}{h} \cdot q_{\text{tr},2\text{D}}^{\ddagger} \cdot q_{\text{rot},3\text{D}}^{\ddagger}, \quad (3)$$

where k_{B} is the Boltzmann constant and h the Planck constant. This formalism is adopted from Minissale et al. (2022), which in turn is based on work by Tait et al. (2005b). In short, TST takes the difference in rotational and translational degrees of freedom between the adsorbed and transition state into account. In equation 3, $q_{\text{tr},2\text{D}}^{\ddagger}$ and $q_{\text{rot},3\text{D}}^{\ddagger}$ are the 2D translational partition function and the 3D rotational partition function, respectively. The 2D translational partition function, because the dimension orthogonal to the surface is assumed to be common to both adsorbed and desorbed molecules. $q_{\text{tr},2\text{D}}^{\ddagger}$ is given by:

$$q_{\text{tr},2\text{D}}^{\ddagger} = \frac{A}{\Lambda^2}. \quad (4)$$

¹ <https://cdms.astro.uni-koeln.de/classic/molecules>

² http://astrochymist.org/astrochymist_mole.html

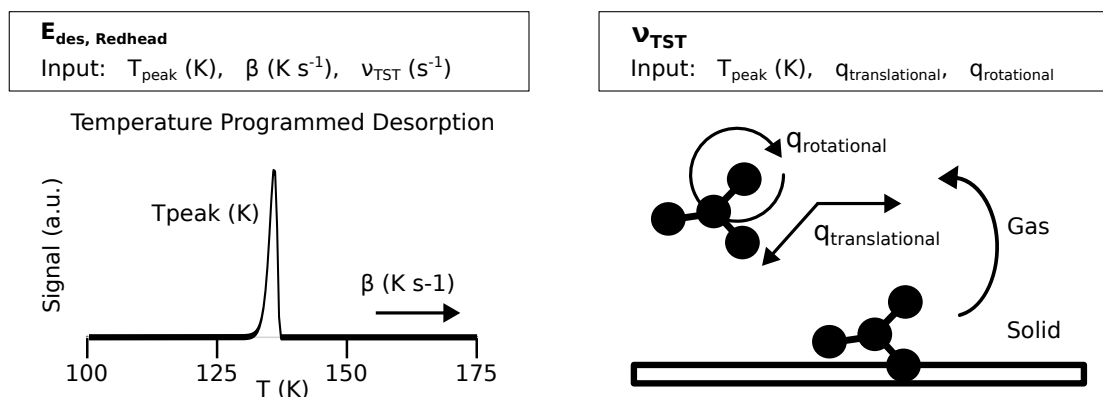


Fig. 1. Visual summary of the Redhead-TST method. The pre-exponential frequency factor (ν) is determined with Transition State Theory (TST). The main input are the translational ($q_{\text{tr},2D}^{\ddagger}$) and rotational ($q_{\text{rot},3D}^{\ddagger}$) partition functions, which increase as the molecule transitions from a solid to gaseous state, and T_{peak} of the molecule. The Redhead equation takes T_{peak} , the heating rate β , and ν_{TST} as main inputs to calculate the desorption energy E_{des} .

The parameter A is the surface area of each adsorbed molecule, which is fixed to 10^{-19} m^2 and is the inverse of the generally assumed number of binding sites (that is, $1 \times 10^{15} \text{ cm}^{-2}$). For large molecules this value could be different, but for simplicity we adopt a uniform value. Λ is the thermal wavelength of the molecule and calculated in the following way:

$$\Lambda = \frac{h}{\sqrt{2 \pi m_{\text{molecule}} k_B T_{\text{peak}}}} \quad (5)$$

In this equation, m_{molecule} is the mass of the particle in kg. Finally, the rotational partition function, $q_{\text{rot},3D}^{\ddagger}$ is given as:

$$q_{\text{rot},3D}^{\ddagger} = \frac{\sqrt{\pi}}{\sigma h^3} \cdot (8\pi^2 k_B T_{\text{peak}})^{3/2} \cdot \sqrt{I_x I_y I_z} \quad (6)$$

Here, σ is the symmetry factor of the molecule and indicates the number of indistinguishable orientations of the particle. I_x , I_y , and I_z are the principal moments of inertia for rotation of the particle. The moments of inertia are determined using a rigid rotor approximation and chemical structures from the ChemSpider³ database. These structures as calculated with a Dreiding force field based geometry optimisation and are not a full quantum mechanical treatment. For a handful of molecules their structures were not available in this database and for these instances they have been calculated with the Avogadro⁴ software. These equations are only applicable to molecules consisting of more than two atoms. Tait et al. (2005b) note that this TST method gives a good approximation of the pre-exponential factor, but can overestimate the value. Adsorbates are assumed to be immobile on the surface and therefore have no rotational or translational degrees of freedom when bound (in other words $q_{\text{ads}} = 1$). Since some molecules are found to migrate on the surface to sites with higher binding energies, they have some degrees of freedom on the surface, which results in $q_{\text{ads}} > 1$. With a mobile adsorbate, $q_{\text{tr},2D}^{\ddagger} \cdot q_{\text{rot},3D}^{\ddagger} / q_{\text{ads}}$ will therefore be lower, thus lowering the pre-exponential factor.

We stress that TST suffers from some limitations. One of the main approximations is that all molecules in the transition state reach the Boltzmann distribution. This could not be the case for

large molecules, and it is the reasons why the TST could fail to treat large molecules. It is not easy to quantitatively define the “large” word but based on the results of the present work and on Minissale et al. (2022), we can tentatively claim that TST starts to fail when the molecule presents more than 20 atoms. Moreover, TST neglects quantum effects, which is important at low temperatures or when the chemical reaction involves tunnelling. We point out that this a second order limitation since, except for H₂ or D₂ or other peculiar cases, desorption occurs at temperature where classical effects overcome of some orders of magnitude quantum effects.

Several species considered in this work are salt complexes, which consist of two molecules that have engaged in an acid-base reaction and are present as a cation-anion pair. For these species, it is generally not possible to determine the moments of inertia and subsequently its pre-exponential factor with TST. To determine the desorption energies of these salts, we take their pre-factor as the sum of the pre-factors of the individual acid and base. The following values are used for individual components: $4.96 \times 10^{15} \text{ s}^{-1}$ for H₂O, $1.63 \times 10^{17} \text{ s}^{-1}$ for HCN, and $1.94 \times 10^{15} \text{ s}^{-1}$ for NH₃ (Minissale et al. 2022) and $2.9 \times 10^{17} \text{ s}^{-1}$ for HNCO, $3.9 \times 10^{17} \text{ s}^{-1}$ for CH₃NH₂, $6.9 \times 10^{19} \text{ s}^{-1}$ for NH₂COOH, $2.0 \times 10^{18} \text{ s}^{-1}$ for HCOOH, $1.3 \times 10^{19} \text{ s}^{-1}$ for CH₃COOH, and $1.7 \times 10^{21} \text{ s}^{-1}$ for the Acetaldehyde Ammonia Trimer (AAT, this work).

2.2. Data set

The data used in this paper have been collected from a wide variety of publications in the laboratory astrochemistry and surface science literature. All these publications make use of TPD experiments in combination with a mass spectrometry technique, such as quadrupole mass spectrometer (QMS) or time-of-flight MS (TOF-MS), to detect and identify molecules.

To determine E_{Redhead} and ν_{TST} , the peak desorption temperature T_{peak} and heating rate β are collected and presented in Table A.2. Table A.1 lists the relevant molecular constants mass, σ , I_x , I_y , and I_z . The heating rate is usually indicated in the publication, but in case β is not provided it is set to 1 K min^{-1} . This matches with most heating rates applied in astrochemical laboratory work, but we note that heating rates in this data set range from 0.1 K min^{-1} to over 1 K s^{-1} . Peak desorption temperatures can textually be indicated in the publication or be determined by-eye from TPD traces presented in figures. The absolute un-

³ <http://www.chemspider.com>

⁴ Avogadro: an open-source molecular builder and visualisation tool. Version 1.2.0 <http://avogadro.cc/>

certainty on the recorded temperature is generally 0.5–2.0 K, depending on the measurement technique used (e.g., thermocouple, diode). However, by-eye analysis of TPD data is inherently more inaccurate and the T_{peak} uncertainty is therefore uniformly set to ± 5 K. Combined with the uncertainties of the equations used, we apply a uniform uncertainty of $\pm 10\%$ on all determined desorption energies.

Table A.2 also lists details about the substrate material, precursor molecules (i.e., starting molecule or mixture of molecules), and the ice processing source. We note that most data are collected for molecules that are formed *in-situ*, instead of as pure or mixed deposited ices. This means that while compositions of the ice at the beginning of the experiment are given, by the time the TPD is started this composition has changed because new molecules have been formed. In fact, some of the listed molecules may form in reactions that are promoted by heating during the TPD. This makes characterising the binding environment of a molecule challenging, as the target molecule does not only interact with the substrate or surrounding precursor species, but potentially with a host of molecules that are formed during processing of the ice. Therefore, when the ice is processed and the target species is formed *in-situ*, the binding environment is assumed to consist of a combination of the substrate material (e.g., metal, carbon, etc) and a residue that is a mix of different and undefined organic molecules. All molecules are assumed to be present at (sub)monolayer coverage ($1\text{ML} \approx 1 \times 10^{15}$ molecules cm^{-2}), unless there is clear mention that multilayer quantities ($\gg 1\text{ML}$) of product are formed, for example determined from IR spectroscopic measurements, in which case the molecule is excluded from the dataset.

It is possible that the molecule under investigation co-desorbs with another matrix species, either a precursor molecule or a new species that is abundantly formed during the processing of the ice. Because co-desorbing species have a peak desorption temperature that is governed by the matrix molecule instead of the binding of the targeted species to the surface, these molecules are excluded from the data set. For precursor molecules (e.g., H_2O , CH_3OH) desorption temperatures are often known and therefore any target molecule that has a T_{peak} close to this is considered to be co-desorbing and excluded. However, during processing new molecules that act as co-desorption matrix can be formed. Because the full molecular inventory is not always described, it is difficult to identify co-desorption in these cases. Only if there is mention or a strong suspicion that co-desorption is occurring the entry is omitted.

A variety of ice processing techniques are used, ranging from UV and X-ray processing to hydrogenation and electron/ion bombardment. We note that thermal processing is also a possibility, but this is only listed when it is explicitly mentioned as a step in the molecule formation process. The TPD process itself is not considered thermal processing.

Finally, data of (sub)monolayer desorption studies presented in the literature have also been collected and are presented in Table A.2 as well. In some cases only v_{lit} and E_{lit} are presented, while in other cases sufficient information is available (i.e., T_{peak} and β) that v_{TST} and E_{Redhead} can also be determined.

3. Results and Discussion

In Table A.2 data of 133 molecules from 132 publications have been collected, for a total of 328 entries. Information on the CHNOPS elemental composition, functional groups, and binding surfaces in the data set are presented in Fig. 2. The vast majority of molecules contain one or more carbon and hydrogen

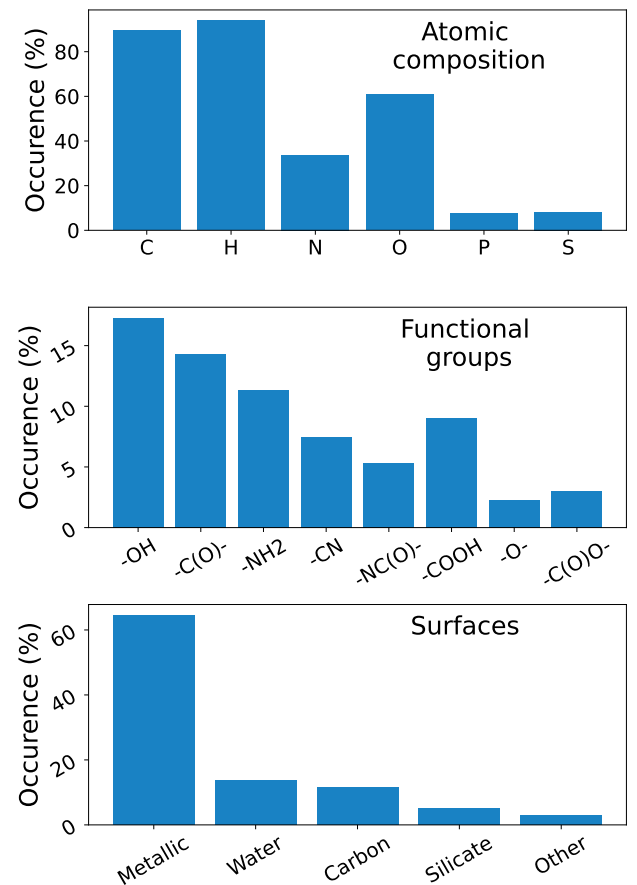


Fig. 2. Occurrences of CHNOPS atoms (top panel), functional groups (middle panel), and binding surfaces (bottom panel) of the entries present in the data set used in this paper. The category “other” in the bottom panel includes surfaces like KBr and MgF_2 windows.

atom, while a substantial fraction contains at least one oxygen atom. About one third of the molecules included contain at least one nitrogen atom, while phosphorus and sulfur are present in a minor percentage of the data set. In terms of functional groups, we find that mostly alcohols, aldehydes or ketones, and amines are covered in the data set. Contrary to what is found in the ISM (e.g., Cernicharo et al. 2020; McGuire et al. 2020; Marcelino et al. 2021; Lee et al. 2021b,a; Loomis et al. 2021; Lee et al. 2022; Cernicharo et al. 2022), cyanides only make up a small portion of this data set and ethers and formates represent the smallest fraction of the functional groups.

This figure highlights the large availability of data experimental data on oxygen-bearing molecules, but relatively few molecules are covered that contain nitrogen, phosphorus, or sulfur atoms. There are two primary explanations for this. First, many precursor molecules with N, P, or S, such as HCN, PH₃, and H₂S, are more difficult to work with in the laboratory or toxic and therefore avoided by experimental researchers. In turn, fewer TPD data on the formation of molecules containing these kind of atoms are available. At the same time the limited amount of data available on N, P, S-bearing species may also indicate that ice chemistry is less efficient at forming such molecules or that molecules containing these atoms are refractory and do not desorb at temperature ≤ 300 K.

Finally, the cold surfaces for these studies are dominated by metallic ones (e.g., Au, Ag, Pt). Surfaces that are more relevant to the ISM, such as crystalline or amorphous water, highly ori-

ented pyrolytic graphite (HOPG), graphene, silica (SiO_2), and silicates (SiO_4^{4-}) make up a smaller percentage of the data set. Only few ice chemistry experiments make use of surface that are not metallic (e.g., Potapov et al. 2022). Since many molecules in the data set are obtained from such experiments, this explains the dominance of metallic surfaces in the data set. However, as mentioned earlier, these molecules are produced *in-situ*, likely together with a mixture of other complex organic molecules that can remain on the surface at temperatures ≥ 300 K. Consequently, the binding surface of the target molecule will be a combination of the metallic surface and an organic molecular residue. This environment be a relevant analogue to dust grains in the ISM, which are presumably coated in a layer of organic molecules once water-ice is removed from their surfaces.

In the following sections a deeper look will be taken at the Redhead-TST method performance and collected desorption energy and pre-exponential factor data.

3.1. Influence of TPD data on the Redhead-TST output

The Redhead-TST method relies on TPD data, which can show major differences in T_{peak} between experiments. Consequently, this influences the derived ν_{TST} and $E_{\text{redhead-TST}}$ values. Examples of this are shown in Fig. 3, where ν_{TST} and $E_{\text{redhead-TST}}$ of all entries of $\text{CH}_3\text{CH}_2\text{CHO}$ (propionaldehyde), $\text{CH}_3\text{COCOCH}_3$ (2,3-Butanedione), NH_2OH (hydroxylamine), $(\text{CH}_2\text{OH})_2$ (ethyleneglycol), HOCHCHOH (1,2-ethenediol), $\text{HOCH}_2\text{CH}(\text{OH})\text{CHO}$ (glyceraldehyde), and $\text{HOCH}(\text{CH}_2\text{OH})_2$ (glycerol) are shown. In all cases, marginal variations of at most one order of magnitude are seen in the pre-exponential factors for each molecule. Variations on this level will have a negligible effect on the simulated desorption profiles. However, in several cases large shifts in the retrieved desorption energy are found, with the most extreme scatter seen in $\text{CH}_3\text{COCOCH}_3$ values, which range from 6920 to 12690 K. These shifts are directly correlated with the peak desorption temperature used as input for the Redhead equation.

The scatter in peak desorption temperatures, and thus desorption energies, has several explanations. First and foremost the coverage of a species of interest is not known in the majority of cases. Therefore, molecules can span a wide range of (sub)monolayer coverages. At lower coverage, molecules have a tendency to settle in deeper binding sites, which have higher desorption energies. Consequently, there is a correlation between coverage and desorption temperature, where lower coverage results in a shift of desorption to higher temperature (see e.g., Smith et al. 2016; He et al. 2016). This effect is more pronounced on rough surfaces, which have a large range of binding sites, like Amorphous Solid Water (ASW) or the organic residue that is presumably formed in the experiments included in this work.

The surface on which the experiment is conducted can also play a role. Almost all entries depicted in Fig. 3 are measured on a metallic surface, but this classification groups many different materials, such as Au, Ag, and Cu, and structure, such as rough, Pt(111), or Mo(110), together. Each metal and surface structure will result in different desorption energies, which in turn shift T_{peak} . This shift is exacerbated when other categories of surfaces are used, such as water ice or carbon. For the selected molecules, a clear example is seen for NH_2OH . One entry is measured on graphite (Ioppolo et al. 2014) and its retrieved desorption energy is a clear outlier with respect to the other entries of this molecule. Similarly, the type of organic residue formed on a surface during an experiment can also influence the desorption characteristics. This is highlighted by $\text{CH}_3\text{COCOCH}_3$,

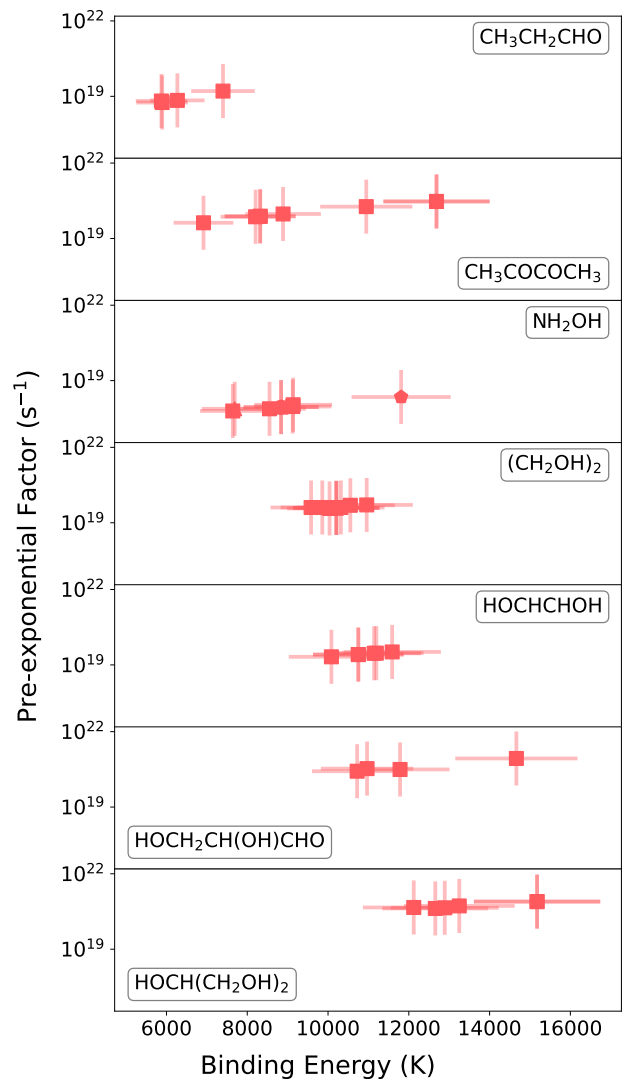


Fig. 3. Values of ν_{TST} and $E_{\text{redhead-TST}}$ of all the entries of $\text{H}_3\text{CH}_2\text{CHO}$ (propionaldehyde), $\text{CH}_3\text{COCOCH}_3$ (2,3-Butanedione), NH_2OH (hydroxylamine), $(\text{CH}_2\text{OH})_2$ (ethyleneglycol), HOCHCHOH (1,2-ethenediol), $\text{HOCH}_2\text{CH}(\text{OH})\text{CHO}$ (glyceraldehyde), and $\text{HOCH}(\text{CH}_2\text{OH})_2$ (glycerol). Symbols indicate a metallic surface (squares) or carbon surface (pentagon, NH_2OH panel).

for which all entries are measured on the same type of Ag surface, but produced with different irradiated precursors, such as CH_3CHO , $\text{CH}_3\text{CHO}:\text{CH}_3\text{COCOCH}_3$, and $\text{H}_2\text{O}:\text{CH}_3\text{CHO}$.

Since the desorption parameters of molecules covered in this study have in most cases not been reported, the values listed in this work can be used as an approximation of the pre-factor and desorption energy, for example in chemical models. However, it is important to be aware that the provided values are limited by the quality of the TPD input data.

3.2. Redhead-TST method performance

In Fig. 4 the Redhead-TST and literature E_{des} and ν values are compared for a number of publications where both these values are available. The top panel of this figure shows the pre-factors values, which are colored based on whether the difference $\Delta(\nu_{\text{TST}} - \nu_{\text{Lit}})$ is smaller than ± 3 orders of magnitude (red squares) or larger than ± 3 orders of magnitude (blue circles). The literature ν values that are in close agreement with their TST counterpart are

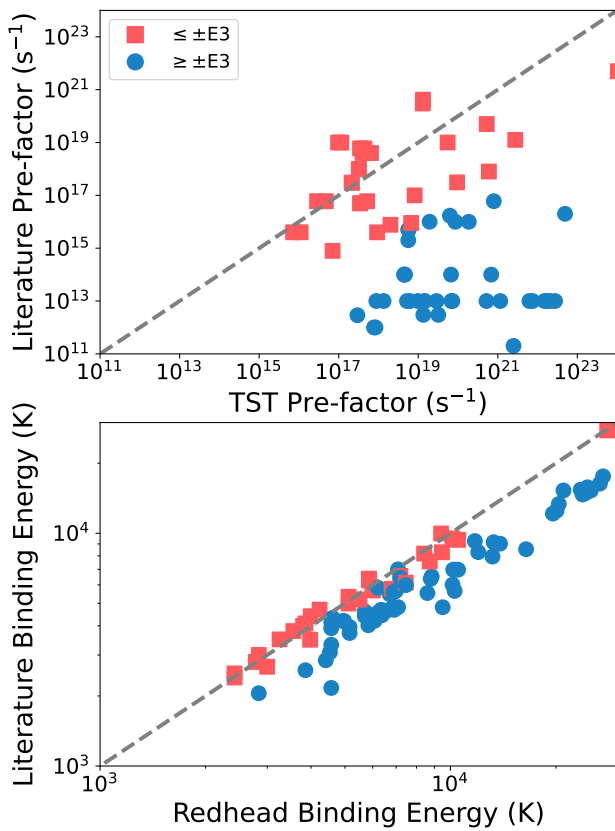


Fig. 4. Comparison between v (top panel) and E_{des} (bottom panel) values obtained from literature sources, but which have also been analysed with the Redhead-TST method. Red squares indicate entries for which the difference between v_{TST} and v_{lit} is smaller than three orders of magnitude, whereas the blue circles indicate those with a difference larger than three orders of magnitude.

found to derive from studies that employ more rigorous methods to determine the pre-factor (e.g., Tait et al. 2005b; Chaabouni et al. 2018; Behmard et al. 2019; Tylinski et al. 2020), although a number of data points are also derived from studies that in fact employ the same TST to calculate v (Ulbricht et al. 2006). To some extent, the large differences in pre-factors are not surprising, as in many studies v is assumed to be 10^{12} or 10^{13} s^{-1} . This tendency is visible in the top panel of Fig. 4. We conclude that the TST method gives accurate approximations of the pre-exponential factor value.

The subsequent effect of the adopted v on the desorption energy is visible in the bottom panel of Fig. 4. The data points in the bottom panel are again labeled according to the difference in pre-factor values. When the difference in v is ≤ 3 decades, the desorption energies are in good agreement and fall on the parity line. Contrary, when there is a large difference between v_{lit} and v_{TST} there is a prominent difference between E_{Redhead} and E_{lit} . Because in all these cases the literature pre-factor is lower than v_{TST} , the corresponding desorption energy is also lower. This comparison shows that the Redhead-TST method gives accurate desorption parameters that are in good agreement with those derived in experiments, provided these experimental parameters are determined with rigorous laboratory and analysis methods.

One may argue that the large discrepancies between $E_{\text{Redhead-TST}}$ and E_{lit} when v_{lit} is assumed will actually not affect the simulated desorption behaviour, as in either case the best fit parameters are generated. An example of this is shown

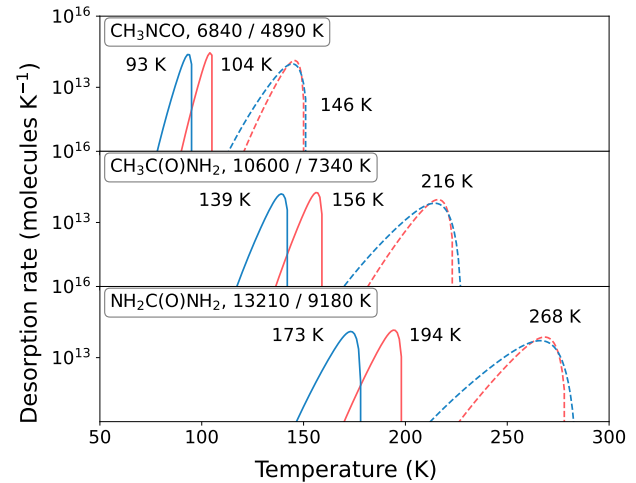


Fig. 5. Desorption traces of CH_3NCO , $\text{CH}_3\text{C}(\text{O})\text{NH}_2$, and $\text{NH}_2\text{C}(\text{O})\text{NH}_2$ with desorption parameters obtained with the Redhead-TST method (red) and the Redhead method, assuming a pre-exponential factor of 10^{13} s^{-1} (blue). Peak desorption temperatures are indicated in the plot for each species. The desorption profile is simulated with a first-order Polanyi-Wigner equation, surface coverage of $1 \times 10^{15} \text{ molecules cm}^{-2}$, and heating rate of 1 K century^{-1} (solid lines), which is appropriate for the ISM, or the heating rate of 5 K min^{-1} (dashed lines) used in these experiments.

in Fig. 5, where data of the molecules CH_3NCO (methyl isocyanate), $\text{CH}_3\text{C}(\text{O})\text{NH}_2$ (acetamide), and $\text{NH}_2\text{C}(\text{O})\text{NH}_2$ (carbamide) are analysed with the Redhead-TST method (red lines) and the Redhead method, while assuming $v = 10^{13} \text{ s}^{-1}$. The dashed lines show the simulated desorption profiles at a heating rate of 5 K min^{-1} , the same temperature ramp as used in the studies where the TPD data of these molecules are taken from (Ligterink et al. 2017, 2018a). The peak desorption temperatures determined with a TST and assumed prefactor are found to be identical and match with the T_{peak} value determined in the laboratory. However, if the heating rate is changed to 1 K century^{-1} , a value that is applicable to interstellar environments, the peak desorption temperatures show a substantial deviation. The simulated profiles with the assumed v value, which are lower than the value determined with TST, underestimate the peak desorption temperature by about 10%. This example highlights the importance of determining desorption parameters, including the pre-exponential factor, as accurately as possible. However, it is important to be aware of the nuances of heating in interstellar environments. Grains can be heated by photons and in the case of very small particles and energetic photons, the grains can be flash heated at rates in the order of K s^{-1} . In these cases desorption energies with assumed pre-exponential factors might be just as applicable, as Fig. 5 shows. In general, it is recommended to use as accurate a value as possible.

3.3. Data trends

Due to the large amount of collected data, it is possible to investigate trends in pre-factor values and desorption energies. In Fig. 6 E_{des} (top panels) and v (bottom panels) are plotted against the molecule mass in amu (left column) and number of atoms of the molecule (right column). Data points obtained with the Redhead-TST method are indicated in red, while those taken from literature are presented in blue. In addition, the recommended desorption parameters of molecules from various surfaces listed in

Minissale et al. (2022) have been added in green points (data from their Table 2 and 3). Each data point is labelled by its surface category, which includes metallic (squares), carbon (pentagons), silicate (triangles), and water-ice (circles).

Both Redhead-TST and literature desorption energies show a general tendency to increase with increasing molecule mass or number of atoms. However, most striking is the large spread in desorption energy values for a given molecular mass or number of atoms, which often spans more than 5000 K (top panels Fig. 6). This spread makes it difficult to retrieve any empirical relationship between the parameters. Even when only data of a specific surface or containing certain functional groups are selected (not shown), no trend or relationship is found.

The situation is different for the pre-exponential factors. While the laboratory literature data is affected by the tendency to assume $\nu = 10^{13} \text{ s}^{-1}$, there is a clear trend in the TST data showing a relationship between ν_{TST} and the molecule mass. These data are fitted with an equation of the form $\log_{10}(\nu) = a \cdot \ln(m) + b$, where m is the mass of the molecule in amu (atomic mass units, and the best-fit values are found to be $a = 2.65$ and of $b = 8.07$. Because both studies make use of Transition State Theory to determine the pre-factor, the data points of both this work (red) and those of Minissale et al. (2022) (green) are used for the fit. The TST data points show a scatter of about one decade around the best-fit line, an uncertainty that has a marginal effect on any simulated desorption profile. The recommended values presented by Minissale et al. (2022) are in good agreement with the found equation and show that the equation can also be used for lower mass molecules. This empirical relationship can be used to estimate the pre-exponential factor of a molecule solely based on its mass. This may find use when analysing laboratory data to determine E_{des} values or as an easy way to determine pre-factors for molecules in astrochemical models (see also Sect. 4.1).

3.4. Desorption parameters and caveats

For several molecules a large number of entries of the same species have been collected in Table A.2. This amount of data can be useful in several cases, such as to analyse the influence of the desorption surface. However, often a single ν and E_{des} value is desired, for example to be used chemical models. The mean values for ν and E_{des} for molecules analysed in this work with the Redhead-TST method are presented Table 1.

It is important to note several caveats of the data provided in Table 1. First, these desorption parameters are the mean of the available data. Monolayer desorption is a more nuanced process and desorption energies will differ depending on coverage and available binding sites. The mean values presented in this table should only be used when no data is available from more rigorous studies and only for specific applications, such as input for astrochemical models.

Second, binding environments are grouped together, but one has to be aware that the desorption energies of these molecules will be different when, for example, amorphous water ice or graphite are considered. The most prominent source of desorption parameter data comes from experiments that make use of metallic surfaces (e.g., Au, Ag, Pt substrates). Often the molecule is formed *in situ* together with other species, and there the binding surface can be seen as a combination of metallic and a refractory organic residue, which makes these environments more realistic.

In connection to the above points, it is important to note that for some molecules extensive studies have been performed

to determine the pure ice (sub)monolayer desorption parameters, including on different surfaces. In particular molecules that are often and abundantly observed in the ISM are on this list, such as CH_3NH_2 , CH_3CHO , HCOOH , $\text{CH}_3\text{CH}_2\text{OH}$, CH_3OCHO , CH_3COOH , and HOCH_2CHO (e.g. Lattelais et al. 2011; Bertin et al. 2011; Burke et al. 2015a,b,c; Chaabouni et al. 2018; Corazzi et al. 2021; Ferrero et al. 2022). While these studies are invaluable to assess the influence of different binding environments, in many cases the pre-exponential frequency factor is assumed (e.g., to be 10^{12} or 10^{13} s^{-1}), which will affect the determined desorption energy. In Table A.2 the Redhead-TST analysis of these data are presented when possible. If desorption parameters on surfaces like amorphous or crystalline water, HOPG, or silicates are required, it is recommended to adopt these values.

While some molecules are well studied, it is also noteworthy that some prominent interstellar molecules have not rigorously been studied in the laboratory, such as dimethyl ether (CH_3OCH_3), ethylene glycol ($(\text{CH}_2\text{OH})_2$), and acetamide ($\text{CH}_3\text{C}(\text{O})\text{NH}_2$). For some molecules like ethylcyanide ($\text{CH}_3\text{CH}_2\text{CN}$) and vinylcyanide (CH_2CHCN) only limited data can be found in the literature (Toumi et al. 2016; Kimber et al. 2018; Couturier-Tamburelli et al. 2018) and only for the case of multilayer desorption. Because these species are routinely observed in the ISM (e.g., Nazari et al. 2022), dedicated laboratory studies of these molecules are desired. The parameters of these molecules presented in this study rely solely on chemical TPD data and should be considered the best currently available.

4. Astrophysical implications

4.1. Impact of the pre-factor on astrochemical models

Astrochemical models make use of the Polanyi-Wigner equation or a variation thereof to calculate the desorption rates of molecules on dust grains (e.g., Kulterer et al. 2020). While for these models desorption energies are generally taken from experimental and theoretical literature, the ν value is calculated with an empirical formula, often the harmonic oscillator relation presented in Hasegawa et al. (1992):

$$\nu = \sqrt{2k_B n_{\text{ss}} E_{\text{des}} / \pi^2 m}, \quad (7)$$

which uses the molecule mass m , the molecule binding energy E_{des} , and the number of binding sites per grain surface area n_{ss} as input to calculate the pre-factor. Except for small molecules and atoms, this equation underestimates the value of ν , often by multiple decades (Minissale et al. 2022). This is also found for molecules considered in this study. Figure 7 shows the difference between ν_{TST} and ν_{Hasegawa} and visualises that for the majority of cases ν_{TST} is at least seven decades larger than the pre-factor calculated with the Hasegawa equation.

The difference in adopted pre-factor can have a strong impact on astrochemical models. Combining a desorption energy that is determined with Redhead-TST or any other accurate method with a pre-factor determined by the Hasegawa equation can severely misrepresent the desorption behaviour of the molecule (see Fig. 2 in Ceccarelli et al. 2022). This is exemplified in Fig. 8 for the molecules CH_3NCO , $\text{CH}_3\text{C}(\text{O})\text{NH}_2$, and $\text{NH}_2\text{C}(\text{O})\text{NH}_2$. For these species $E_{\text{Redhead-TST}}$ is determined with data from Ligterink et al. (2017) and Ligterink et al. (2018a) and subsequently plotted with ν_{TST} (red) and ν_{Hasegawa} (blue). The desorption profiles (left panel) plotted with ν_{Hasegawa} are all

Table 1. Mean desorption parameters.

Molecule	ν	E_{des}	$T_{\text{peak,ISM}}^a$	Molecule	ν	E_{des}	$T_{\text{peak,ISM}}$
	s^{-1}	K	K		s^{-1}	K	K
C ₂ H ₄	9.1e+15	2602	45	CH ₃ CHCHOH	1.6e+19	8330	125
C ₂ H ₆	4.8e+16	2773	46	CH ₃ OCH ₂ OH	1.9e+19	8471	127
C ₃ H ₈	6.5e+17	3721	59	(CH ₃) ₂ NCHO	6.7e+19	8785	129
CH ₂ CHCH ₃	3.9e+17	3709	60	[NH ₄ ⁺][OCN ⁻]	2.9e+17	8117	129
CH ₃ PH ₂	4.4e+17	4662	74	CH ₃ OCH ₂ CH ₃	2.1e+19	8633	129
CH ₃ I	9.3e+17	4758	75	C ₆ H ₅ CCH	1.1e+20	8915	130
CH ₃ CCH	1.9e+17	4624	75	CH ₃ CH ₂ CH ₂ OH	3.8e+19	8909	132
C ₄ H ₁₀	5.7e+18	4946	76	c-C ₃ H ₂ O	5.8e+18	8766	133
CH ₃ CHO	9.7e+17	4882	77	C ₆ H ₅ CHO	3.0e+20	9502	136
H ₂ SO ₂	2.6e+18	5035	78	CH ₂ CH(OH)CH ₃	3.3e+19	9415	139
H ₂ CCO	1.7e+17	4895	79	CH ₃ COCOCH ₃	1.4e+20	9621	139
N ₂ H ₂	5.9e+16	4891	81	NH ₂ OH	1.0e+18	8954	140
c-C ₃ H ₄ O	2.9e+18	5319	82	[NH ₄ ⁺][CH ₃ COO ⁻]	1.3e+19	9408	141
HNCO	2.9e+17	5154	83	NH ₂ CH ₂ CN	2.4e+19	9529	142
CH ₂ NH	5.3e+16	5106	84	CH ₃ CH ₂ C ₆ H ₅	5.3e+20	10126	144
CH ₃ OOCH ₃	4.2e+18	5560	86	H ₂ PCOOH	6.4e+19	9852	144
CH ₃ CHCH ₂ O	4.4e+18	5715	88	c-H ₂ C ₃ O	1.2e+19	9605	144
CH ₃ CH ₂ OCHO	1.6e+19	5833	88	H ₂ POH	3.0e+18	9446	145
CH ₃ OCHO	4.7e+18	5715	88	[NH ₄ ⁺][HCOO ⁻]	2.0e+18	9426	145
CH ₃ NC	2.9e+17	5657	91	NH ₂ CH(CH ₃)OH	4.2e+19	9910	146
NO ₂	3.7e+17	5676	91	C ₁₀ H ₂₂	2.7e+21	10517	146
HCOPH ₂	3.7e+18	6006	92	CH ₃ CH ₂ CH ₂ SH	9.6e+19	10070	147
CH ₃ CH ₂ NH ₂	2.3e+18	6033	94	c-NCHCH ₂	4.3e+18	9733	148
P ₂ H ₄	2.2e+18	6183	96	CH ₃ OOCOH	6.6e+19	10151	149
CH ₃ NH ₂	4.9e+17	6025	96	HOCH ₂ OH	1.1e+19	9911	149
CH ₃ CH ₂ CHO	8.8e+18	6359	97	CH ₂ CHCH ₂ OH	3.3e+19	10139	150
HCOSH	3.8e+18	6301	97	(CH ₂ OH) ₂	4.2e+19	10214	151
CH ₃ COCH ₃	1.0e+19	6459	98	[CH ₃ NH ₃ ⁺][NCO ⁻]	6.8e+17	9688	152
CH ₃ CHNH	1.9e+18	6327	98	HOCH ₂ NH ₂	1.2e+19	10138	152
CH ₂ CHNH ₂	1.9e+18	6326	98	CH ₂ C(OH)COOH	1.5e+20	10578	153
H ₃ SiC(H)CO	7.9e+18	6439	98	C ₁₀ H ₈	5.7e+20	10831	154
C ₆ H ₁₄	8.5e+19	6874	101	HOCH ₂ CN	3.0e+19	10375	154
CH ₃ P ₂ H ₃	1.4e+19	6675	101	HCOCOOH	7.8e+19	10838	158
CH ₃ SH	1.8e+18	6522	101	CH ₃ NHCHO	3.1e+19	10708	158
CH ₃ OCH ₃	2.0e+18	6503	101	CH ₃ CONH ₂	4.0e+19	10763	159
H ₂ S ₂	2.8e+18	6560	101	CH ₃ COCOOH	1.9e+20	11169	161
CH ₃ NCO	6.8e+18	6842	104	H ₂ CC(OH) ₂	3.4e+19	10985	162
c-C ₆ H ₁₂	6.3e+19	7187	106	(CH ₂ -O)x	4.5e+17	10267	162
HC ₂ CHO	4.3e+18	6957	107	HOCHCHOH	2.7e+19	10918	162
CH ₂ CHOH	2.1e+18	6957	108	c-C ₆ H ₅ CN	4.1e+20	11628	166
N ₂ H ₄	4.4e+17	6779	108	C ₆ H ₅ CHCH ₂	1.1e+21	12136	170
CH ₂ CHCHO	8.1e+18	7162	109	HOCH ₂ CH(OH)CHO	4.4e+20	12034	171
(CHO) ₂	6.2e+18	7163	109	C ₆ H ₁₅ N ₃	1.7e+21	12279	171
(CH ₃) ₂ C ₆ H ₄	1.4e+20	7457	109	H ₂ CO ₃	5.3e+19	12160	178
C ₄ H ₄ S	5.0e+19	7492	111	[NH ₄ ⁺][NH ₂ COO ⁻]	6.9e+19	12166	178
HCOOH	2.0e+18	7135	111	C ₁₄ H ₁₀	3.2e+21	13019	180
[H ₃ O ⁺][OCN ⁻]	3.0e+17	7087	113	HOCH ₂ COOH	1.6e+20	12730	184
CH ₃ CH ₂ OH	5.2e+18	7400	113	CH ₃ P(O)(OH) ₂	2.5e+20	13241	190
CH ₃ C ₆ H ₅	4.2e+19	7698	114	HOCH(CH ₂ OH) ₂	5.7e+20	13545	192
C ₆ H ₆	1.2e+19	7710	116	NH ₂ COOH	6.9e+19	13276	194
CH ₃ COOH	1.3e+19	7680	116	NH ₂ CONH ₂	3.4e+19	13284	196
CH ₃ C(O)OCH ₃	4.1e+19	7807	116	[C ₆ H ₁₅ N ₃ H ⁺][HCOO ⁻]	1.7e+21	14186	198
HOCH ₂ CHO	1.6e+19	7797	117	NH ₂ CH ₂ COOH	3.2e+20	14390	205
HCCNH ₂	1.6e+18	7587	118	S ₃	2.8e+20	14846	212
[NH ₄ ⁺][CN ⁻]	1.6e+17	7417	119	S ₄	8.3e+20	15497	218
CHOCH ₂ CN	2.8e+19	8099	120	H ₂ P(O)OH	8.2e+19	15207	221
CH ₂ OCHCN	2.8e+19	8099	120	CH ₃ SCH ₃	1.1e+20	15350	222
CH ₃ OOH	4.2e+18	7845	120	C ₅ H ₆ N ₂ O ₂	6.4e+21	20232	276
(CH ₂ NH ₂) ₂	1.9e+19	8097	121	C ₂₄ H ₁₂	4.9e+22	21013	279
CH ₃ COCN	3.3e+19	8125	121	C ₄ H ₅ N ₃ O	1.7e+22	23675	318
P ₃ H ₅	4.4e+19	8227	122	C ₅ H ₅ N ₅	1.5e+22	23812	320
C ₈ H ₁₈	6.0e+20	8728	124	C ₅ H ₅ N ₅ O	3.2e+22	26209	348
PH ₂ CH ₂ PH ₂	2.8e+19	8307	124	C ₃₂ H ₁₄	1.0e+24	28012	356
HCCOH	1.2e+18	8029	125	C ₆₀	4.1e+24	33634	399

Notes. Molecules are sorted by increasing T_{peak} value. ^aThe T_{peak} is determined from a desorption profile simulated with a first-order Polanyi-Wigner equation, surface coverage of 1×10^{15} molecules cm⁻², and heating rate of 1 K century⁻¹. Note that these mean values in many cases consists of a superposition of binding environments, many of which are not relevant to interstellar environments (i.e. metallic surfaces). These values should be taken as best available.

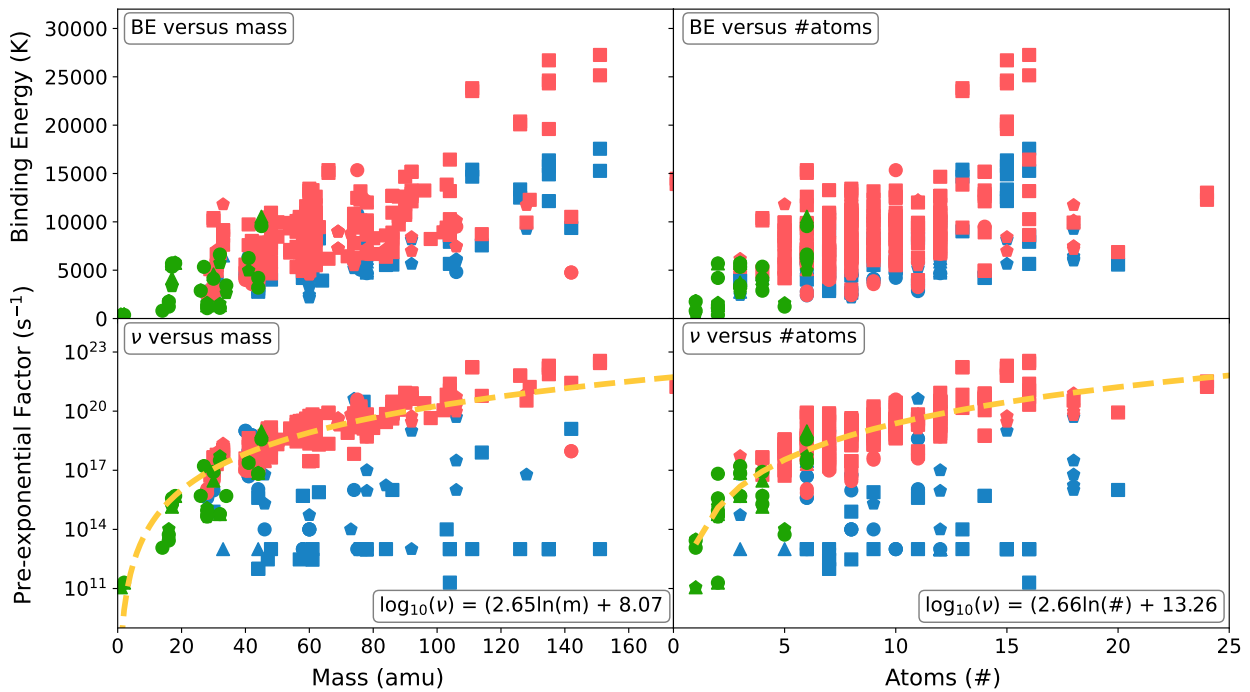


Fig. 6. Desorption energy (top row) and pre-exponential factor (bottom row) plotted against molecule mass (left column) and number of atoms (right column). Values derived with the Redhead-TST method are coloured in red, recommended desorption parameters adopted from Minissale et al. (2022) in green, and other literature sources are presented in blue. Marker symbol indicates whether a molecule is desorbing from a metallic (squares), water (circles), silicate (triangle), or carbon (pentagon) surface.

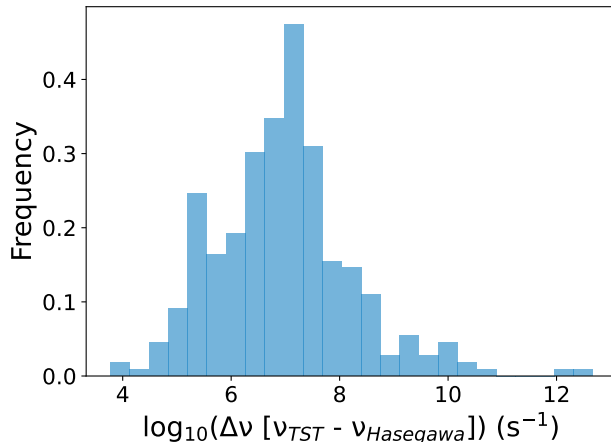


Fig. 7. Difference between ν_{TST} and $\nu_{Hasegawa}$ for molecules presented in this study. Frequencies normalised to one are presented.

shifted to higher temperatures and misrepresent the actual desorption profile. For these examples the peak desorption temperature is about 30% higher than what it should be. In the right panel the gas and ice column densities are plotted against the radius of a protoplanetary disk, which has the average temperature profile $T(r) = 200 \times (r/1AU)^{0.62}$ K, as found by Andrews & Williams (2007). For each 1 K temperature step, the number of desorbed molecules is determined, which summed give the gas-phase column density and subtracted from a starting value of 1×10^{15} cm $^{-2}$ give the ice column density. As expected from their peak desorption temperatures, the ice-gas inversion point lies at a larger radius when the accurate TST pre-factor is used. Using $\nu_{Hasegawa}$ results in the inversion point shifting $\sim 50\%$ inwards.

Due to its impact on astrochemical models, it is recommended to use more accurate pre-exponential factor values. One way is to implement the empirical equation presented in Sect. 3.3, with the caveat that this equation is ill suited to determine pre-factors for atoms and diatomic molecules. Better yet is to use the ν and E_{des} that belong together as presented in the literature source as direct input for the chemical model, to prevent any misrepresentation.

4.2. Peak desorption temperatures

For simplicity and consistency, desorption profiles and peak desorption temperatures are calculated using Eq. 1 and a heating rate of 1 K century $^{-1}$ in this work. However, this heating rate is not appropriate for all interstellar environments and peak desorption temperatures are often determined with other equations, such as the adsorption-thermal-desorption balance presented by Hasegawa et al. (1992) (see also Nazari et al. 2021):

$$\frac{n_{ice}}{n_{gas}} = \frac{\pi a_{grain}^2 n_{grain} \sqrt{3k_B T m^{-1}}}{e^{-E_{des}/T} \sqrt{2k_B n_{ss} E_{des} \pi^{-2} m^{-1}}}. \quad (8)$$

As input, this equation takes the grain size a_{grain} (set to 0.1 μ m), the grain number density n_{grain} (set to 1.0×10^{-12} n_H, with n_H the gas density), the sticking efficiency S (set to 1), the gas and grain temperature T, the molecule mass m, the molecule binding energy E_{des} , and the number of binding sites per grain surface area n_{ss} to calculate the ice-to-gas ratio. The peak desorption temperature is taken as the point where ice and gas molecular abundances are equal, that is $n_{ice} / n_{gas} = 1$. Instead of the peak desorption temperature depending on the heating rate values, in this equation it primarily depends on the gas density of the

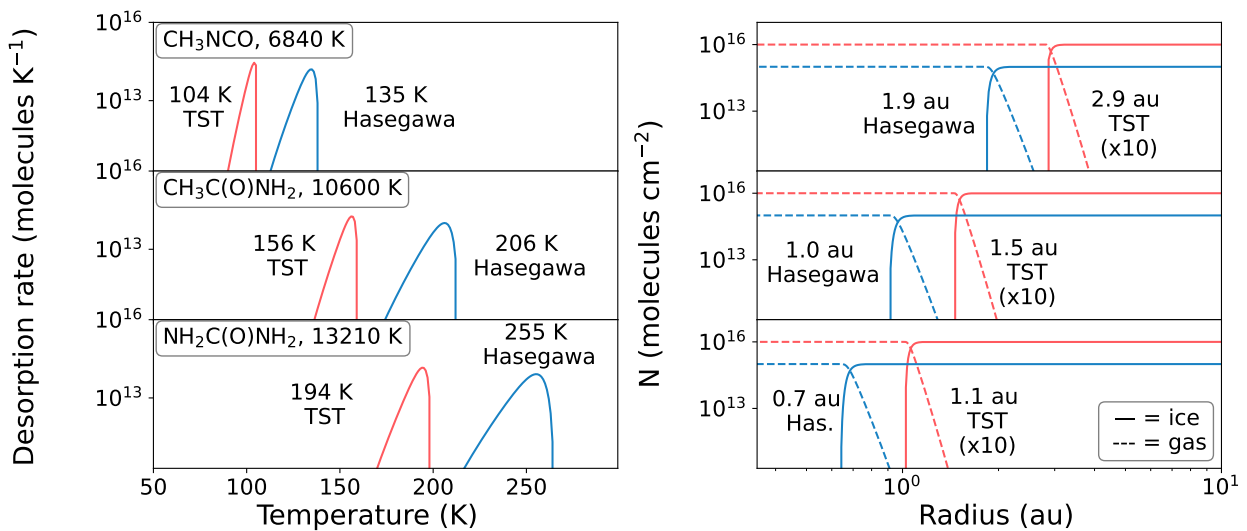


Fig. 8. Comparison of desorption profiles generated with the TST (red) or the Hasegawa (blue) prefactor. Left panel: desorption profiles of CH₃NCO, CH₃C(O)NH₂, and NH₂C(O)NH₂. The desorption energies are determined with the Redhead-TST method using data from Ligterink et al. (2017) and Ligterink et al. (2018a) (see Table A.2 and top left corners). Desorption profiles are plotted for ν_{TST} (red) and with ν_{Hasegawa} (blue). The desorption profile is simulated with a first-order Polanyi-Wigner equation, surface coverage of 1×10^{15} molecules cm⁻², and heating rate of 1 K century⁻¹. Peak desorption temperatures decrease by ~30% when realistic pre-factors are used. Right panel: ice (solid) and gas (dashed) abundances plotted against radius (au) of a protoplanetary disk for ν_{TST} (red) and with ν_{Hasegawa} (blue). An average disk temperature profile of $T(r) = 200 \times (r/1AU)^{0.62}$ K is used (Andrews & Williams 2007). For each 1 K temperature step, the number of desorbed molecules is determined, which summed give the gas-phase column density and subtracted from a starting value of 1×10^{15} cm⁻² give the ice column density. The TST abundances are offset by a factor of 10 for easier viewing. The peak radii of the ice-gas inversion are indicated and are shown to shift outward by ~50% when realistic pre-factors are used.

environment. Furthermore, we note that this equation in its original form makes use of the harmonic oscillator relation to calculate the pre-exponential frequency in the denominator. As discussed Sect. 4.1, this equation gives inaccurate values for larger molecules and therefore the equation should rather take accurate pre-factor into account:

$$\frac{n_{\text{ice}}}{n_{\text{gas}}} = \frac{\pi a_{\text{grain}}^2 n_{\text{grain}} \sqrt{3k_B T m^{-1}}}{\nu_{\text{TST}} e^{-E_{\text{des}}/T}}. \quad (9)$$

Using the latter equation, the peak desorption temperatures where calculated for $n_{\text{H}} = 1 \times 10^7$ cm⁻³ (appropriate for molecular clouds) and $n_{\text{H}} = 1 \times 10^{12}$ cm⁻³ (appropriate for protoplanetary disk environments) and compared with the T_{peak} determined from the peak of the Polanyi-Wigner desorption profile using a heating rate of $\beta = 1$ K century⁻¹. Desorption parameters listed in Table 1 were used. In Table 2 the results for a selection of twenty molecules are presented.

The adsorption-thermal-desorption equation at low density ($n_{\text{H}} = 1 \times 10^7$ cm⁻³) shows a small difference with the Polanyi-Wigner results. One aspect that affects this comparison is the definition of the peak desorption temperature of the adsorption-thermal-desorption balance equation, which is located at the point where $n_{\text{ice}} / n_{\text{gas}} = 1$. However, for the T_{peak} from the Polanyi-Wigner equation this is usually $n_{\text{ice}} / n_{\text{gas}} \leq 0.1$. Correcting for this discrepancy raises the adsorption-thermal-desorption balance peak desorption temperatures by several K. In turn, this make $T_{\text{peak,PW}}$ and $T_{\text{peak,ATD}}$ for the low-density scenario virtually identical. Quite different is the situation for the high-density ($n_{\text{H}} = 1 \times 10^{12}$ cm⁻³) results of the adsorption-thermal-desorption balance equation, which show peak desorption temperatures that are approximately 20% higher than those obtained with the Polanyi-Wigner equation. The peak desorption temperatures listed in this study might therefore not be representative

for all interstellar environments and source-specific modelling is required to accurately determine desorption fronts.

4.3. Salt desorption

Several molecules detected in the interstellar medium can be classified as acids ([AH], e.g., HCOOH, HNCO, CH₃COOH) or bases ([B], e.g., NH₃, CH₃NH₂). In ice mantles, these species can engage in acid-base reactions and form organic salts via the reaction [AH] + [B] \rightarrow [A⁻][BH⁺]. Several of such salts are included in this study and their desorption energies are determined. The pre-factors of these salts are determined by adding the pre-exponential factor values of its individual components ([AH] and [B]), see Sect. 2.1. While there is a chemical diversity in the salts, they often include ammonia as the base. In the interstellar medium, ammonia is also expected to be a prominent base, due to its high ice abundance (up to 10% w.r.t. H₂O, Boogert et al. 2015). In all cases, E_{des} of the salt is larger than the value of its individual components and therefore the salts will reside on dust grains at higher temperatures (see also e.g., Kruczakiewicz et al. 2021). This is exemplified in Fig. 9 where the desorption profiles of various salts and their corresponding acid and base are plotted. A first-order Polanyi-Wigner equation is used, with a monolayer coverage of 10^{15} molecules cm⁻² and a heating rate of 1 K century⁻¹. Differences in peak desorption temperatures range from just over 10 K for the H₂O-HNCO system, to more than 60 K for the CH₃NH₂-HNCO system.

The ability to lock up molecules in the form of salts can have number of implications. Large quantities of organic molecules with amino (-NH₂) or carboxylic acid (-COOH) groups can be trapped in organic salt complexes and remain on dust grains and larger bodies at elevated temperatures. Recent analysis of samples collected and return from the asteroid Ryugu show that it contains high concentrations of amines (e.g., CH₃NH₂) and

Table 2. Comparison peak desorption temperatures.

Molecule	$T_{p,PW}$	$T_{p,ATD}$	Diff.	$T_{p,ATD}$	Diff.
		$n_{H,7}$		$n_{H,12}$	
	K	K	%	K	%
C_2H_4	45	43	96	54	119
CH_3CHO	77	75	98	92	119
H_2CCO	79	78	98	95	120
CH_2NH	84	83	99	102	121
CH_3SH	101	100	99	121	120
CH_3OCH_3	101	99	98	121	120
CH_3NCO	104	102	98	124	119
HC_2CHO	107	105	98	127	119
CH_2CHOH	108	106	98	129	120
$(CHO)_2$	109	107	99	130	119
$HCOOH$	111	109	98	133	119
CH_3CH_2OH	113	111	99	135	120
CH_3COOH	116	114	98	138	119
NH_2OH	140	139	99	169	121
H_2PCOOH	144	143	99	172	119
$HOCH_2CN$	154	152	99	184	119
$HCOCOOH$	158	157	99	188	119
NH_2CONH_2	196	195	99	235	120
S_4	218	216	99	258	118
C_{60}	399	417	104	487	122

Notes. Peak desorption temperatures for various molecules, using the Polanyi-Wigner equation ($T_{p,PW}$, with $\beta = 1 \text{ K century}^{-1}$), and the adsorption-thermal-desorption equation ($T_{p,ATD}$), for $n_H = 1 \times 10^7 \text{ cm}^{-3}$ ($n_{H,7}$) and $n_H = 1 \times 10^{12} \text{ cm}^{-3}$ ($n_{H,12}$). The differences between the adsorption-thermal-desorption and Polanyi-Wigner peak desorption temperatures are indicated in percent of ($T_{p,ATD} / T_{p,PW}$). Desorption parameters from Table 1 are used.

acids ($HCOOH$ and CH_3COOH , Naraoka et al. 2023). Because these molecules are found to not be trapped in minerals or other organic matter, the authors suggest that these species reside in the material as salts in order to explain why these volatiles are still present. Our results underline this conclusion, although questions remains if the salts included in this study, which are still relatively volatile, could have survived the heating ($\geq 300 \text{ K}$) and hydrothermal stages during the formation of Ryugu (Nakamura et al. 2022). Further desorption studies of salts complexes could help unravel in which salt form amines and acids are locked up in asteroid Ryugu.

Organic salt complexes also provide a molecular reservoir that remains available for grain surface chemistry for a longer time (or rather to higher temperatures) but not for gas-phase reactions. Ammonia is the dominant nitrogen carrier in observed interstellar ice, but it is also relatively volatile. Locking ammonia up in ammonium salts (NH_4^+) could mean that a substantial atomic nitrogen reservoir is available on interstellar grains long after NH_3 or H_2O have desorbed, see Fig. 9. Laboratory investigations of the processing of salts with energetic radiation at elevated temperatures ($\geq 100 \text{ K}$) and in water-free environments, are relevant avenues to investigate the formation of prebiotic molecules (see for example Bossa et al. 2009b).

As salts desorb at higher temperatures, they can give misleading indications of sublimation fronts as determined with observations of interstellar environments. For example, Lee et al. (2022) measure the spatial distribution of various molecules toward the HH212 protoplanetary disk and find similar radial distributions of $HNCO$ and NH_2CHO . If the presence of these molecules in the gas can entirely be explained by ice desorption,

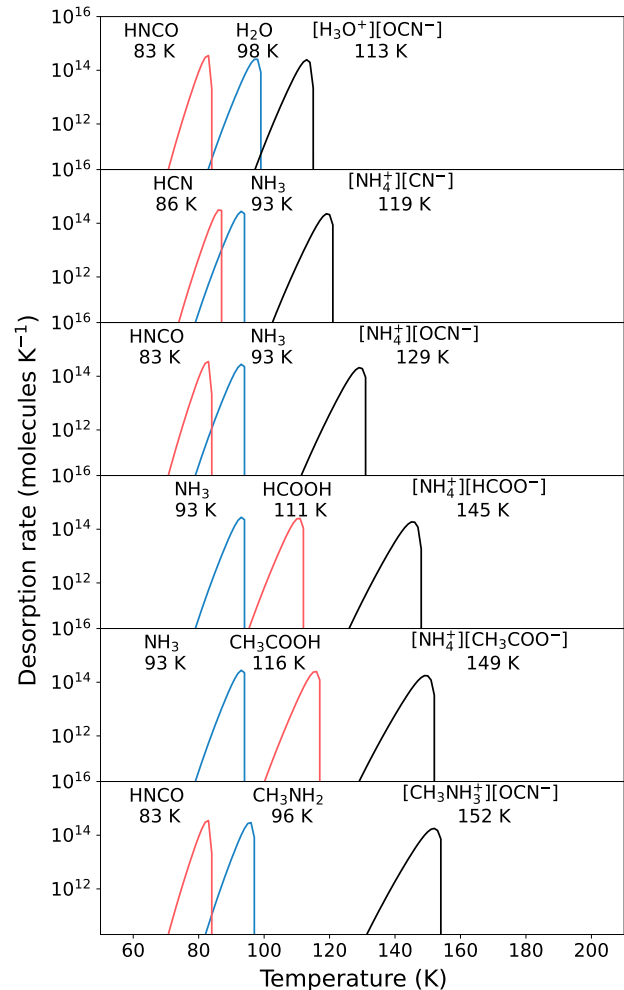


Fig. 9. Desorption profiles of acids (red), bases (blue), and the resulting salt (black). Desorption energies and pre-factors for H_2O , NH_3 , and HCN are obtained from Minissale et al. (2022), while the parameters for the remaining molecules are taken from Table 1. Peak desorption temperatures are indicated in the plot for each species. The desorption profile is simulated with a first-order Polanyi-Wigner equation, surface coverage of $10^{15} \text{ molecules cm}^{-2}$, and heating rate of 1 K century^{-1} .

this co-spatial distribution is peculiar as these molecules have significantly different desorption parameters of $2.9 \times 10^{17} \text{ s}^{-1}$ and 5154 K (this work) and $3.69 \times 10^{18} \text{ s}^{-1}$ and 9561 K (Minissale et al. 2022) for $HNCO$ and NH_2CHO , respectively. One would expect that $HNCO$ desorbs at a much lower temperature or larger radius than NH_2CHO . However, if instead most of the $HNCO$ available in the ice has reacted with NH_3 , it would be locked up in the $[NH_4^+][OCN^-]$ salt. This salt has the desorption parameters $2.9 \times 10^{17} \text{ s}^{-1}$ and 8117 K , which are close to those of formamide. The salt can therefore explain the co-spatial distribution of $HNCO$ and NH_2CHO due to thermal desorption of the $[NH_4^+][OCN^-]$ salts, which upon desorption dissociates into its individual components, $HNCO$ and NH_3 (see also Lee et al. 2022).

Thus far two molecules have been detected in the interstellar medium that are presumed to be part of salt complexes. These are the cyanate anion (OCN^-) and the ammonium cation NH_4^+ (Lacy et al. 1984; Keane et al. 2001; Pontoppidan et al. 2003; Van Broekhuizen et al. 2005). Recently, these species have also been detected in observations with the new *James Webb Space Telescope* (JWST, McClure et al. 2023). The unprecedented sen-

sitivity of JWST opens up two avenues of research. First, it is possible to look for other salt components at lower abundance or with weaker spectroscopic features, for example the cyanide anion (CN^-) and carboxylate anions ($\text{R}-\text{COO}^-$). Second, searches for salts in water poor or free interstellar environments, for example molecular clouds that interact with the warm gas of a protostellar outflow or the edges of photo dominated regions (PDRs), can be conducted. Because the bulk ice species have been removed from the grains in these regions, the less abundant salt and organic species are easier to detect. Furthermore, the presence and shape of salt spectroscopic signatures will provide information about the chemical and physical history of the environment.

4.4. Chemical and elemental composition above the water-snow line

Within star- and planet-forming environments temperature gradients and the associated desorption fronts of molecules, also called snow lines, play an important role in forming planetary objects and setting their chemical and elemental composition. Examples of such lines are the nitrogen and water snowline or the soot line, which is driven by the sublimation of large carbon-dominated molecules such as polycyclic aromatic hydrocarbons (PAHs). These lines are invoked to explain the high atomic nitrogen abundance in Jupiter or the comparatively low carbon content of Earth (Bosman et al. 2019; Öberg & Bergin 2021; Li et al. 2021). Because of their high abundances, observational, modelling, and experimental efforts have focused on the main ice species to investigate desorption fronts. Since most organic molecules except for CH_3OH and CH_4 are found at low abundances, these species will not affect the elemental composition of a protoplanetary disk or create snow lines that are observable. However, the combined inventory of organic molecules may affect the elemental composition. *ISO* and *Spitzer* IR observation of various interstellar sources have found significant features in the 5–8 μm region (Gibb & Whittet 2002; Boogert et al. 2008). These features have at least in part been assigned to an organic residue consisting of a variety of molecules, including HCOOH and HCOO^- . Therefore, the data presented in this paper are used in this section to investigate how a large reservoir of diverse organic molecules affects elemental ratios and the chemical composition, for example in a protoplanetary disk.

Elemental ratios of hydrogen, nitrogen, oxygen, phosphorus, and sulphur over carbon are determined for a molecular inventory that consists of the species listed in this work and desorption parameters presented in Table 1, supplemented by bulk ice species with parameters taken from Table 3 of Minissale et al. (2022). The ice abundances are set with respect to water. The following fractions are used: CO , N_2 , and CO_2 at 0.25, CH_3OH at 0.1, O_2 , CH_4 , NH_3 , and H_2CO at 0.05, and H_2S , CS , and HCN at 0.01. Combined, the aforementioned species are indicated as the bulk ice species. All remaining organic molecules listed in this work, as well as C_2H_2 , CH_3CN , NH_2CHO taken from Minissale et al. (2022) are included in a low and high fraction scenario where each organic molecule contributes at 10^{-4} and 10^{-3} level, respectively. The desorption profile, including ice and gas abundances are simulated with a first-order Polanyi-Wigner equation, variable abundances according to fractions with respect to water, and a heating rate of 1 K century $^{-1}$. The elemental composition is obtained by multiplying the ice or gas abundance of each molecule with its elemental composition (e.g., for CH_3OH carbon = abundance \times 1, hydrogen = abundance \times 4, and oxygen =

abundance \times 1) and subsequently summing all contributions to an element.

The resulting ice elemental compositions for [Hydrogen]/[Carbon], [Nitrogen]/[Carbon], [Oxygen]/[Carbon], and [Sulphur]/[Carbon] are shown in Fig. 10. Figure B.1 in the Appendix shows the same plot, but with elemental ratios plotted versus protoplanetary disk radius by using an average protoplanetary disk temperature profile $T(r) = 200 \times (r/1\text{AU})^{0.62}$ K (Andrews & Williams 2007). The elemental ratio of [Phosphorus]/[Carbon] is shown in Fig. B.2 in the Appendix. The bulk ice elemental ratios are plotted in blue, while the addition of a low ($10^{-4} \times [\text{H}_2\text{O}]$) and high ($10^{-3} \times [\text{H}_2\text{O}]$) fraction of organic molecules are plotted in red and green, respectively. The peak desorption temperatures of several bulk ice species are indicated, as well as the elemental composition of the extraterrestrial substances Soluble Organic Matter (SOM, Sephton 2002) and Insoluble Organic Matter (IOM, Alexander et al. 2017). Both SOM and IOM are regularly extracted from meteorites and SOM shows similarities with the organic material measured on several solar system objects, such as comet 67P/ Churyumov-Gerasimenko (Hänni et al. 2022). In this work, we use the average elemental composition of $\text{C}_{100}\text{H}_{155}\text{N}_3\text{O}_{20}\text{S}_3$ for SOM obtained from the Murchison meteorite (Schmitt-Kopplin et al. 2010) and the average IOM composition of $\text{C}_{100}\text{H}_{77}\text{O}_{14}\text{N}_3\text{S}_2$ presented in Alexander et al. (2017).

First, we note that the addition of organic material affects the elemental ratios at low temperatures, when bulk ice dominates. The combined contribution of organic elemental carbon lowers all elemental ratios. The effect is most pronounced for the high fraction organic matter model where it can lower ratios by up to 100%. In this scenario we only take the contribution of the 133 molecules studied in this work into account. In a natural environment the diversity of the organic components may be many times larger (e.g., Hänni et al. 2022) and therefore have an even larger impact on elemental ratios.

Second, we note the importance of the organic material to set the ice elemental composition when the bulk ice species are removed from the solid state. In our model, all the bulk ice species are lost before ~ 115 K, while the species that contribute to the nitrogen and sulphur budget are gone at lower temperatures of ~ 100 K and ~ 75 K, respectively. These differences in bulk ice desorption explain the dips seen in [N]/[C] and [S]/[C] between 75 and 100 K. At these points the nitrogen (NH_3) and sulphur (CS) reservoirs have desorbed, but the main carrier of carbon (CH_3OH) is still present. It is likely that these dips will be less pronounced in reality due to the trapping of the volatile nitrogen and sulphur carriers in the dominating water-phase, which desorbs together methanol. After desorption of the bulk ice reservoir the organic material starts to dominate the overall elemental composition on the dust grains.

The elemental ratios are biased towards the molecules included in this work and the assumption that molecules contribute equally to the total molecular budget is unlikely to be realistic. Therefore, care needs to be taken with any interpretation of Fig. 10. However, some general observations can be made. First, at low temperature (≤ 115 K) or larger radii (≥ 3 au), the bulk ices dominate the elemental budget and ratios are seen to vary in a stepwise manner. Objects formed in this regime will have predictable elemental compositions, depending on the “step” they form at. However, in the warmer disk regions closer to the (proto)star and where water has desorbed, the elemental budget is set by the large mixture of organic molecules, which desorb at different temperatures. Consequently, the elemental composition is seen to be much more varied, especially in [Hy-

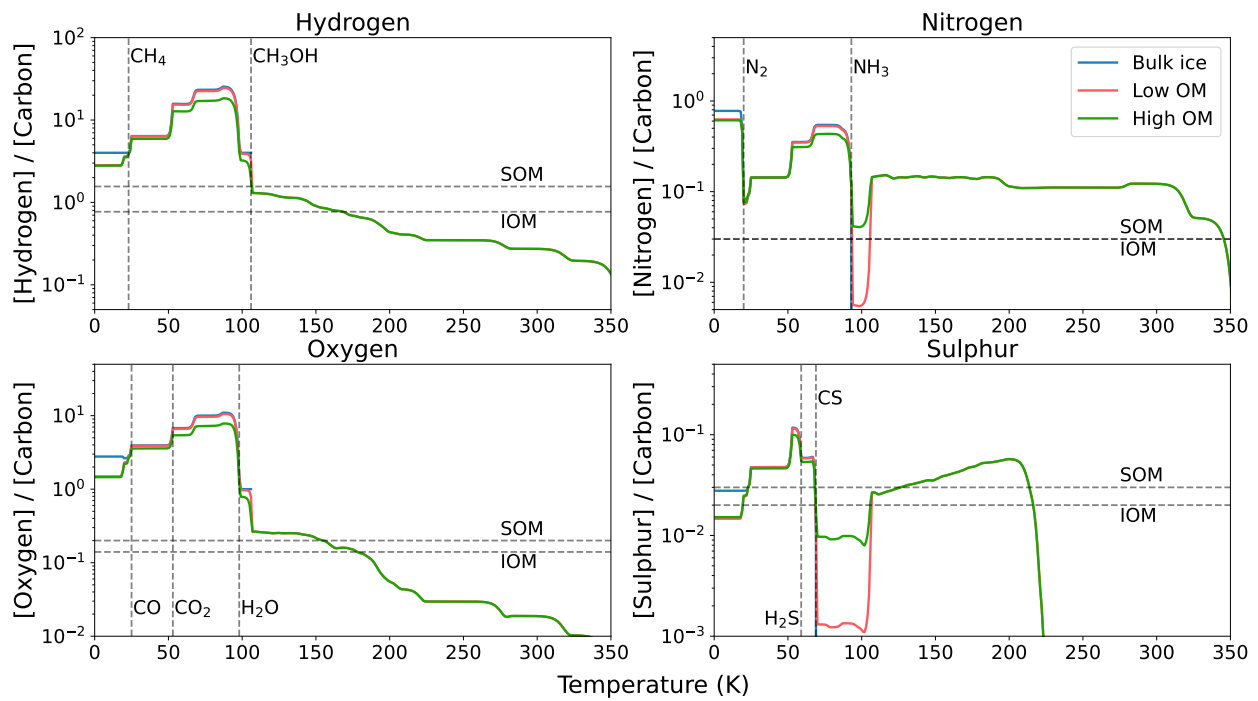


Fig. 10. Ice elemental composition as $[X]/[\text{Carbon}]$ for Hydrogen, Nitrogen, Oxygen, and Sulphur as a function of temperature. Peak desorption temperatures for selected species are indicated in the plot (vertical dashed lines). Elemental compositions of Soluble Organic Matter (SOM) obtained from the Murchison meteorite (Schmitt-Kopplin et al. 2010) and averaged Insoluble Organic Matter (IOM, Alexander et al. 2017) are indicated (horizontal dashed lines). The desorption profiles are simulated with a first-order Polanyi-Wigner equation, variable surface coverages, and a heating rate of 1 K century^{-1} . Low and high OM represent low and high fraction of organic molecules, respectively.

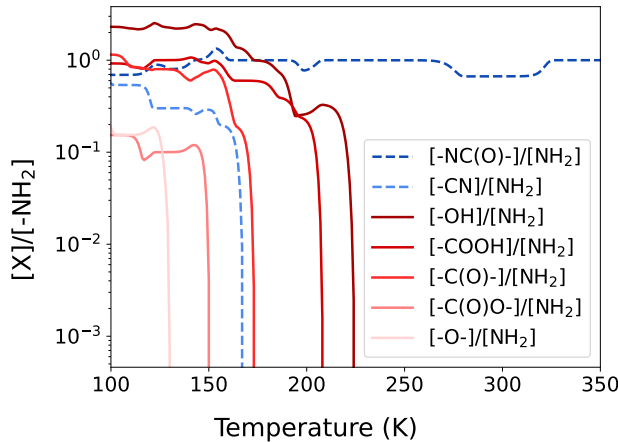


Fig. 11. Functional chemical group composition $[X]/[-\text{NH}_2]$ for oxygen-bearing groups $-\text{OH}$, $-\text{COOH}$, $-\text{C}(\text{O})-$, $-\text{C}(\text{O})\text{O}-$, and $-\text{O}-$ (solid red lines) and nitrogen-bearing groups $-\text{NC}(\text{O})-$ and $-\text{CN}$ (dashed blue lines) as a function of temperature. The desorption profiles are simulated with a first-order Polanyi-Wigner equation, variable surface coverages, and a heating rate of 1 K century^{-1} .

drogen]/[Carbon] and [Oxygen]/[Carbon]. Objects that form in this regime could thus be expected to have a much more varied or less predictable elemental signature.

It is interesting to point out that the organic molecules that remain on the grains at $T \geq 100 \text{ K}$ show similarities with, and in some cases are identical to, the molecules used by Kudo et al. (2002) to determine the sticking velocity of organics-coated grains. These authors found that organics-coated grains rapidly coagulate in the $2.3 - 3.0 \text{ au}$ region of a disk. This region is in

good agreement with the location where we find most organic molecules still coating the grains after water has desorbed.

Finally, the evolution of various functional chemical groups are plotted in Fig. 11. The abundances of the functional groups have been determined in the same way that the elemental abundances have. Ratios of amides ($[-\text{NC}(\text{O})-]/[-\text{NH}_2]$), cyanides ($[-\text{CN}]/[-\text{NH}_2]$), alcohols ($[-\text{OH}]/[-\text{NH}_2]$), carboxylic acids ($[-\text{COOH}]/[-\text{NH}_2]$), aldehydes + ketones ($[-\text{C}(\text{O})-]/[-\text{NH}_2]$), esters ($[-\text{C}(\text{O})\text{O}-]/[-\text{NH}_2]$), and ethers ($[-\text{O}-]/[-\text{NH}_2]$) with respect to amines ($[-\text{NH}_2]$) are plotted. This plot reflects several observations already made in Sect. 3 about the occurrence in of certain functional groups in the data set, for example that the alcohol ($-\text{OH}$) group is most abundant. It also shows that some of these functional groups can be quickly depleted as the environment warms up. In particular esters and ethers will be removed quickly. On the other hand, amides and amines seem to remain present to higher temperatures. In this way we see how chemical make-up and average properties of an organics-coated grain may change with temperature and could potentially be used as a tracers of thermal history of a particle in the solar system. However, it is important to acknowledge that this view is biased towards relatively small and volatile organic molecules. For example, IOM is rich in ether ($-\text{O}-$) cross links (Remusat et al. 2005) and because this substance is very refractory it will ensure that the ether functional group will remain prominent component of the organic coating of grains at elevated temperatures.

5. Conclusion

This study presents a large number of desorption parameters, that is desorption energies (E_{des}) and pre-exponential frequency factors (ν). These parameters will find use in astrochemical models and help to understand the evolution of the chemical and elemental composition in star and planet-forming regions. Because the

list of molecules is dominated by organic molecules and salts of medium-volatility these data are of particular importance to assess the surface chemistry in regions where water ice has been removed from dust grains.

To expand the number of molecules for which desorption parameters are available, experimental temperature programmed desorption data have been collected from the literature and analysed with the Redhead Transition State Theory (Redhead-TST) method to determine the pre-exponential frequency factor (ν) and the desorption energy (E). A comparison with literature ν and E_{des} values shows that the Redhead-TST method provides reliable results that are on par with results of rigorous experimental methods. We emphasise that the usage of accurately determined pre-factor values, instead of assumed values or the often used Hasagawa equation, is essential to properly simulate the desorption profiles of molecules. Due to the large amount of data collected in this study, trends can be searched for. No relationship between molecule mass or number of atoms is found, but a relationship between the pre-factor and molecule mass in the form of $\log_{10}(\nu) = 2.65\ln(m) + 8.07$ is, which can be used to determine this parameter in future studies. Mean desorption parameters are provided and used to highlight how the desorption of these species can affect chemical and elemental compositions.

Acknowledgements. The authors thank E.F. van Dishoeck, E.G. Bøgelund, and C. Ceccarelli for helpful discussions and feedback. Thanks go out to K.-J. Chuang for making unpublished TPD plots of CH_2CHNH_2 and CH_3CHNH available for analysis. The authors thank the many astrochemists and surface scientists who have contributed data to the literature on which this study relies. N.F.W.L. acknowledges support from the Swiss National Science Foundation (SNSF) Ambizione grant 193453 and NCCR PlanetS. M.M. acknowledges the French national programme “Physique et Chimie du Milieu Interstellaire” (PCMI) of CNRS/INSU with INC/INP cofunded by CEA and CNES.

References

- Abplanalp, M. J., Borsuk, A., Jones, B. M., & Kaiser, R. I. 2015, *ApJ*, 814, 45
 Abplanalp, M. J., Förstel, M., & Kaiser, R. I. 2016, *Chem. Phys. Lett.*, 644, 79
 Abplanalp, M. J., Frigge, R., & Kaiser, R. I. 2019, *Sci. Adv.*, 5, eaaw5841
 Abplanalp, M. J. & Kaiser, R. I. 2019, *PCCP*, 21, 16949
 Alexander, C. O., Cody, G., De Gregorio, B., Nittler, L., & Stroud, R. 2017, *Geochemistry*, 77, 227
 Altwegg, K., Balsiger, H., Bar-Nun, A., et al. 2016, *Sci. Adv.*, 2, e1600285
 Andrews, S. M. & Williams, J. P. 2007, *ApJ*, 659, 705
 Bahr, S. & Kempfer, V. 2007, *J. Chem. Phys.*, 127, 074707
 Behmard, A., Fayolle, E. C., Graninger, D. M., et al. 2019, *ApJ*, 875, 73
 Bergantini, A., Abplanalp, M. J., Pokhilko, P., et al. 2018a, *ApJ*, 860, 108
 Bergantini, A., Frigge, R., & Kaiser, R. I. 2018b, *ApJ*, 859, 59
 Bergantini, A., Göbi, S., Abplanalp, M. J., & Kaiser, R. I. 2018c, *ApJ*, 852, 70
 Bergantini, A., Zhu, C., & Kaiser, R. I. 2018d, *ApJ*, 862, 140
 Bergner, J. B., Öberg, K. I., Rajappan, M., & Fayolle, E. C. 2016, *ApJ*, 829, 85
 Bertin, M., Doronin, M., Fillion, J.-H., et al. 2017, *A&A*, 598, A18
 Bertin, M., Romanzin, C., Michaut, X., Jeseck, P., & Fillion, J.-H. 2011, *J. Phys. Chem. C*, 115, 12920
 Bertrand, T., Lellouch, E., Holler, B., et al. 2022, *Icarus*, 373, 114764
 Bianchi, E., López-Sepulcre, A., Ceccarelli, C., et al. 2022, *The Astrophysical Journal Letters*, 928, L3
 Bisschop, S., Fuchs, G., Boogert, A., Van Dishoeck, E., & Linnartz, H. 2007, *A&A*, 470, 749
 Boamah, M. D., Sullivan, K. K., Shulenberger, K. E., et al. 2014, *Faraday Discuss.*, 168, 249
 Bøgelund, E. G., Barr, A. G., Taquet, V., et al. 2019, *A&A*, 628, A2
 Boogert, A. A., Gerakines, P. A., & Whittet, D. C. 2015, *ARA&A*, 53, 541
 Boogert, A. C., Pontoppidan, K. M., Knez, C., et al. 2008, *The Astrophysical Journal*, 678, 985
 Bosman, A. D., Criddle, A. J., & Miguel, Y. 2019, *A&A*, 632, L11
 Bossa, J., Theule, P., Duvernay, F., & Chiavassa, T. 2009a, *ApJ*, 707, 1524
 Bossa, J.-B., Borget, F., Duvernay, F., et al. 2012, *Aust. J. Chem.*, 65, 129
 Bossa, J.-B., Duvernay, F., Theulé, P., et al. 2009b, *A&A*, 506, 601
 Bovolenta, G. M., Vogt-Geisse, S., Bovino, S., & Grassi, T. 2022, *ApJS*, 262, 17
 Burke, D., Wolff, A., Edridge, J., & Brown, W. 2008, *J. Chem. Phys.*, 128, 104702
 Burke, D. J. & Brown, W. A. 2010, *PCCP*, 12, 5947
 Burke, D. J., Puletti, F., Brown, W. A., et al. 2015a, *MNRAS*, 447, 1444
 Burke, D. J., Puletti, F., Woods, P. M., et al. 2015b, *J. Phys. Chem. A*, 119, 6837
 Burke, D. J., Puletti, F., Woods, P. M., et al. 2015c, *J. Chem. Phys.*, 143, 164704
 Butscher, T., Duvernay, F., Danger, G., & Chiavassa, T. 2016, *A&A*, 593, A60
 Carrascosa, H., Cruz-Díaz, G., Muñoz Caro, G. M., Dartois, E., & Chen, Y. 2020, *MNRAS*, 493, 821
 Ceccarelli, C., Codella, C., Balucani, N., et al. 2022, arXiv preprint arXiv:2206.13270
 Cernicharo, J., Fuentetaja, R., Cabezas, C., et al. 2022, *A&A*, 663, L5
 Cernicharo, J., Marcelino, N., Agúndez, M., et al. 2020, *A&A*, 642, L8
 Chaabouni, H., Baouche, S., Diana, S., & Minissale, M. 2020, *A&A*, 636, A4
 Chaabouni, H., Diana, S., Nguyen, T., & Dulieu, F. 2018, *A&A*, 612, A47
 Chuang, K.-J., Fedoseev, G., Qasim, D., et al. 2020, *A&A*, 635, A199
 Congiu, E., Fedoseev, G., Ioppolo, S., et al. 2012, *ApJL*, 750, L12
 Corazzi, M. A., Brucato, J. R., Poggiali, G., et al. 2021, *ApJ*, 913, 128
 Coupeaud, A., Piétri, N., Allouche, A., Aycard, J.-P., & Couturier-Tamburelli, I. 2008, *J. Phys. Chem. A*, 112, 8024
 Couturier-Tamburelli, I., Toumi, A., Piétri, N., & Chiavassa, T. 2018, *Icarus*, 300, 477
 Danger, G., Borget, F., Chomat, M., et al. 2011a, *A&A*, 535, A47
 Danger, G., Bossa, J.-B., De Marcellus, P., et al. 2011b, *A&A*, 525, A30
 Danger, G., Duvernay, F., Theulé, P., Borget, F., & Chiavassa, T. 2012, *ApJ*, 756, 11
 Danger, G., Rimola, A., Abou Mrad, N., et al. 2014, *PCCP*, 16, 3360
 De Jong, A. & Niemantsverdriet, J. 1990a, *Vacuum*, 41, 232
 De Jong, A. & Niemantsverdriet, J. 1990b, *Surf. Sci.*, 233, 355
 Demers, L. M., Östblom, M., Zhang, H., et al. 2002, *J. Am. Chem. Soc.*, 124, 11248
 DeSimone, A. J., Olanrewaju, B. O., Grieves, G. A., & Orlando, T. M. 2013, *J. Chem. Phys.*, 138, 084703
 Dostert, K.-H., O'Brien, C. P., Mirabella, F., Ivars-Barceló, F., & Schauermann, S. 2016, *PCCP*, 18, 13960
 Duvernay, F., Danger, G., Theulé, P., Chiavassa, T., & Rimola, A. 2014, *ApJ*, 791, 75
 Duvernay, F., Dufauret, V., Danger, G., et al. 2010, *A&A*, 523, A79
 Eckhardt, A. K., Bergantini, A., Singh, S. K., Schreiner, P. R., & Kaiser, R. I. 2019, *Angew. Chem.*, 131, 5719
 Fedoseev, G., Chuang, K.-J., Ioppolo, S., et al. 2017, *ApJ*, 842, 52
 Fedoseev, G., Chuang, K.-J., van Dishoeck, E. F., Ioppolo, S., & Linnartz, H. 2016, *MNRAS*, 460, 4297
 Fedoseev, G., Cuppen, H. M., Ioppolo, S., Lamberts, T., & Linnartz, H. 2015a, *MNRAS*, 448, 1288
 Fedoseev, G., Ioppolo, S., Zhao, D., Lamberts, T., & Linnartz, H. 2015b, *MNRAS*, 446, 439
 Ferrero, S., Grieco, F., Ibrahim Mohamed, A., et al. 2022, *MNRAS*, 516, 2586
 Förstel, M., Bergantini, A., Maksyutenko, P., Göbi, S., & Kaiser, R. I. 2017, *ApJ*, 845, 83
 Förstel, M., Maksyutenko, P., Jones, B., et al. 2016a, *Chemical Commun.*, 52, 741
 Förstel, M., Tsegaw, Y. A., Maksyutenko, P., et al. 2016b, *ChemPhysChem*, 17, 2726
 Fray, N. & Schmitt, B. 2009, *Planetary and Space Science*, 57, 2053
 Frigge, R., Zhu, C., Turner, A. M., et al. 2018a, *ApJ*, 862, 84
 Frigge, R., Zhu, C., Turner, A. M., et al. 2018b, *Chemical Commun.*, 54, 10152
 Garrod, R. T., Jin, M., Matis, K. A., et al. 2022, *The Astrophysical Journal Supplement Series*, 259, 1
 Germain, A., Tinacci, L., Pantaleone, S., Ceccarelli, C., & Ugliengo, P. 2022, *ACS Earth Space Chem.*, 6, 1286
 Gibb, E. & Whittet, D. 2002, *The Astrophysical Journal*, 566, L113
 Goesmann, F., Rosenbauer, H., Bredehöft, J. H., et al. 2015, *Sci.*, 349, aab0689
 Gorai, P., Bhat, B., Sil, M., et al. 2020, *ApJ*, 895, 86
 Guennoun, Z., Couturier-Tamburelli, I., Piétri, N., & Aycard, J.-P. 2005, *J. Phys. Chem. B*, 109, 3437
 Hänni, N., Altwegg, K., Combi, M., et al. 2022, *Nat. Commun.*, 13, 1
 Hasegawa, T. I., Herbst, E., & Leung, C. M. 1992, *ApJS*, 82, 167
 He, J., Acharyya, K., & Vidali, G. 2016, *ApJ*, 825, 89
 He, J., Vidali, G., Lemaitre, J.-L., & Garrod, R. T. 2015, *ApJ*, 799, 49
 Heyl, J., Holdship, J., & Viti, S. 2022, *ApJ*, 931, 26
 Hsu, S.-Y., Liu, S.-Y., Liu, T., et al. 2022, *The Astrophysical Journal*, 927, 218
 Ioppolo, S., Fedoseev, G., Chuang, K.-J., et al. 2021, *Nature Astronomy*, 5, 197
 Ioppolo, S., Fedoseev, G., Minissale, M., et al. 2014, *PCCP*, 16, 8270
 Ioppolo, S., Van Boheemen, Y., Cuppen, H., Van Dishoeck, E., & Linnartz, H. 2011, *MNRAS*, 413, 2281
 Jimenez-Escobar, A. & Muñoz Caro, G. 2011, *The Molecular Universe*, 280, 153
 Jin, M. & Garrod, R. T. 2020, *The Astrophysical Journal Supplement Series*, 249, 26
 Johnson, P. E., Young, L. A., Protopapa, S., et al. 2021, *Icarus*, 356, 114070
 Jones, B. M., Kaiser, R. I., & Strazzulla, G. 2014, *ApJ*, 788, 170
 Kaiser, R. I. & Maksyutenko, P. 2015, *Chem. Phys. Lett.*, 631, 59

- Keane, J., Tielens, A., Boogert, A., Schutte, W., & Whittet, D. 2001, *A&A*, 376, 254
- Kimber, H. J., Toscano, J., & Price, S. D. 2018, *MNRAS*, 476, 5332
- King, D. A. 1975, *Surf. Sci.*, 47, 384
- Kleimeier, N. F., Abplanalp, M. J., Johnson, R. N., et al. 2021a, *ApJ*, 911, 24
- Kleimeier, N. F., Eckhardt, A. K., & Kaiser, R. I. 2021b, *J. Am. Chem. Soc.*, 143, 14009
- Kleimeier, N. F., Eckhardt, A. K., Schreiner, P. R., & Kaiser, R. I. 2020a, *Chem.*, 6, 3385
- Kleimeier, N. F. & Kaiser, R. I. 2021, *J. Phys. Chem. Lett.*, 13, 229
- Kleimeier, N. F., Turner, A. M., Fortenberry, R. C., & Kaiser, R. I. 2020b, *ChemPhysChem*, 21, 1531
- Kruczakiewicz, F., Vitorino, J., Congiu, E., Theulé, P., & Dulieu, F. 2021, *A&A*, 652, A29
- Kudo, T., Kouchi, A., Arakawa, M., & Nakano, H. 2002, *Meteoritics & Planetary Science*, 37, 1975
- Kulterer, B. M., Drozdovskaya, M. N., Coutens, A., Manigand, S., & Stéphan, G. 2020, *MNRAS*, 498, 276
- Lacy, J., Baas, F., Allamandola, L., et al. 1984, *ApJ*, 276, 533
- Lasne, J., Laffon, C., & Parent, P. 2012, *PCCP*, 14, 697
- Lattelais, M., Bertin, M., Mokrane, H., et al. 2011, *A&A*, 532, A12
- Layssac, Y., Gutiérrez-Quintanilla, A., Chiavassa, T., & Duvernay, F. 2020, *MNRAS*, 496, 5292
- Lee, C.-F., Codella, C., Ceccarelli, C., & López-Sepulcre, A. 2022, *ApJ*, 937, 10
- Lee, K. L. K., Changala, P. B., Loomis, R. A., et al. 2021a, *ApJL*, 910, L2
- Lee, K. L. K., Loomis, R. A., Burkhardt, A. M., et al. 2021b, *ApJL*, 908, L11
- Leroux, K., Guillemin, J.-C., & Krim, L. 2021, *MNRAS*, 507, 2632
- Li, J., Bergin, E. A., Blake, G. A., Ciesla, F. J., & Hirschmann, M. M. 2021, *Sci. Adv.*, 7, eabd3632
- Ligterink, N., Ahmadi, A., Coutens, A., et al. 2021, *A&A*, 647, A87
- Ligterink, N., Coutens, A., Kofman, V., et al. 2017, *MNRAS*, 469, 2219
- Ligterink, N., Terwisscha van Scheltinga, J., Taquet, V., et al. 2018a, *MNRAS*, 480, 3628
- Ligterink, N. F., Ahmadi, A., Luitel, B., et al. 2022, *ACS Earth Space Chem.*, 6, 455
- Ligterink, N. F., El-Abd, S. J., Brogan, C. L., et al. 2020, *ApJ*, 901, 37
- Ligterink, N. F. W., Calcutt, H., Coutens, A., et al. 2018b, *A&A*, 619, A28
- Liu, G., Rodriguez, J., Chang, Z., Hrbek, J., & González, L. 2002, *J. Phys. Chem. B*, 106, 9883
- Loomis, R. A., Burkhardt, A. M., Shingledecker, C. N., et al. 2021, *Nature Astronomy*, 5, 188
- Mahjoub, A., Poston, M. J., Blacksberg, J., et al. 2017, *ApJ*, 846, 148
- Maity, S., Kaiser, R. I., & Jones, B. M. 2014a, *Faraday Discuss.*, 168, 485
- Maity, S., Kaiser, R. I., & Jones, B. M. 2014b, *Faraday Discuss.*, 168, 485
- Maity, S., Kaiser, R. I., & Jones, B. M. 2015, *PCCP*, 17, 3081
- Maksyutenko, P., Martín-Doménech, R., Piacentino, E. L., Öberg, K. I., & Rajappan, M. 2022, *ApJ*, 940, 113
- Marcelino, N., Tercero, B., Agúndez, M., & Cernicharo, J. 2021, *A&A*, 646, L9
- Marks, J. H., Wang, J., Evseev, M. M., et al. 2023, *ApJ*, 942, 43
- McClure, M. K., Rocha, W., Pontoppidan, K., et al. 2023, *Nature Astronomy*, 1
- McGuire, B. A. 2022, *The Astrophysical Journal Supplement Series*, 259, 30
- McGuire, B. A., Burkhardt, A. M., Loomis, R. A., et al. 2020, *ApJL*, 900, L10
- McManus, J. R., Martono, E., & Vohs, J. M. 2014, *Catal. Today*, 237, 157
- Minissale, M., Aikawa, Y., Bergin, E., et al. 2022, *ACS Earth Space Chem.*, 6, 597
- Minissale, M. & Dulieu, F. 2014, *J. Chem. Phys.*, 141, 014304
- Muir, M., Molina, D. L., Islam, A., Abdel-Rahman, M. K., & Trenary, M. 2020, *PCCP*, 22, 25011
- Mumma, M. J. & Charnley, S. B. 2011, *ARA&A*, 49, 471
- Nakamura, T., Matsumoto, M., Amano, K., et al. 2022, *Science*, eabn8671
- Naraoka, H., Takano, Y., Dworkin, J. P., et al. 2023, *Science*, 379, eabn9033
- Nazari, P., Meijerhof, J., van Gelder, M., et al. 2022, *A&A*, 668, A109
- Nazari, P., van Gelder, M., Van Dishoeck, E., et al. 2021, *Astronomy & Astrophysics*, 650, A150
- Noble, J., Diana, S., & Dulieu, F. 2015, *MNRAS*, 454, 2636
- Noble, J., Theule, P., Duvernay, F., et al. 2014, *PCCP*, 16, 23604
- Oba, Y., Watanabe, N., Kouchi, A., Hama, T., & Pirronello, V. 2010, *ApJ*, 722, 1598
- Öberg, K. I. & Bergin, E. A. 2021, *Physics Reports*, 893, 1
- Östblom, M., Liedberg, B., Demers, L. M., & Mirkin, C. A. 2005, *J. Phys. Chem. B*, 109, 15150
- Peck, J. W., Mahon, D. I., & Koel, B. E. 1998, *Surf. Sci.*, 410, 200
- Piacentino, E. L. & Öberg, K. I. 2022, *ApJ*, 939, 93
- Pontoppidan, K., Fraser, H., Dartois, E., et al. 2003, *A&A*, 408, 981
- Potapov, A., Fulvio, D., Krasnokutski, S., Jäger, C., & Henning, T. 2022, *J. Phys. Chem. A*, 126, 1627
- Potapov, A., Theulé, P., Jäger, C., & Henning, T. 2019, *ApJL*, 878, L20
- Qasim, D., Fedoseev, G., Chuang, K.-J., et al. 2019, *A&A*, 627, A1
- Redhead, P. 1962, *vacuum*, 12, 203
- Remusat, L., Derenne, S., Robert, F., & Knicker, H. 2005, *Geochimica et Cosmochimica Acta*, 69, 3919
- Rubin, M., Altweig, K., Balsiger, H., et al. 2019, *MNRAS*, 489, 594
- Rzeźnicka, I. I., Lee, J., Maksymovych, P., & Yates, J. T. 2005, *J. Phys. Chem. B*, 109, 15992
- Salter, T. L., Stubbing, J. W., Brigham, L., & Brown, W. A. 2018, *J. Chem. Phys.*, 149, 164705
- Salter, T. L., Wootton, L., & Brown, W. A. 2019, *ACS Earth Space Chem.*, 3, 1524
- Schaff, J. E. & Roberts, J. T. 1994, *J. Phys. Chem.*, 98, 6900
- Schaff, J. E. & Roberts, J. T. 1998, *Langmuir*, 14, 1478
- Schmitt-Kopplin, P., Gabelica, Z., Gougeon, R. D., et al. 2010, *PNAS*, 107, 2763
- Schneider, H., Caldwell-Overdier, A., Coppitiers 't Wallant, S., et al. 2019, *Monthly Notices of the Royal Astronomical Society: Letters*, 485, L19
- Schwane, A., Fieberg, J. E., & White, J. 1997, *J. Phys. Chem. B*, 101, 11112
- Sephton, M. A. 2002, *Natural product reports*, 19, 292
- Sexton, B., Hughes, A., & Avery, N. 1985, *Surf. Sci.*, 155, 366
- Singh, S. K., Zhu, C., La Jeunesse, J., Fortenberry, R. C., & Kaiser, R. I. 2022, *Nat. Commun.*, 13, 1
- Slayton, R., Aubuchon, C., Camis, T., Noble, A., & Tro, N. 1995, *J. Phys. Chem.*, 99, 2151
- Smith, R. S. & Kay, B. D. 2018, *J. Phys. Chem. B*, 122, 587
- Smith, R. S., May, R. A., & Kay, B. D. 2016, *J. Phys. Chem. B*, 120, 1979
- Solomon, T., Christmann, K., & Baumgärtel, H. 1989, *J. Phys. Chem.*, 93, 7199
- Souda, R. 2011, *J. Chem. Phys.*, 135, 164703
- Sullivan, K. K., Boamah, M. D., Shulmenberger, K. E., et al. 2016, *MNRAS*, 460, 664
- Tait, S. L., Dohnálek, Z., Campbell, C. T., & Kay, B. D. 2005a, *J. Chem. Phys.*, 122, 164707
- Tait, S. L., Dohnálek, Z., Campbell, C. T., & Kay, B. D. 2005b, *J. Chem. Phys.*, 122, 164708
- Tarczay, G., Förstel, M., Göbi, S., Maksyutenko, P., & Kaiser, R. I. 2017, *ChemPhysChem*, 18, 882
- Theulé, P., Borget, F., Mispelaer, F., et al. 2011a, *A&A*, 534, A64
- Theulé, P., Borget, F., Mispelaer, F., et al. 2011b, *A&A*, 534, A64
- Thrower, J., Collings, M., Rutten, F., & McCoustra, M. 2009, *J. Chem. Phys.*, 131, 244711
- Tinacci, L., Germain, A., Pantaleone, S., et al. 2022, *ACS Earth Space Chem.*, 6, 1514
- Toumi, A., Piétri, N., Chiavassa, T., & Couturier-Tamburelli, I. 2016, *Icarus*, 270, 435
- Tsegaw, Y. A., Göbi, S., Förstel, M., et al. 2017, *J. Phys. Chem. A*, 121, 7477
- Turner, A. M., Abplanalp, M. J., Bergantini, A., et al. 2019, *Sci. Adv.*, 5, eaaw4307
- Turner, A. M., Abplanalp, M. J., & Kaiser, R. I. 2016, *ApJ*, 819, 97
- Turner, A. M., Bergantini, A., Abplanalp, M. J., et al. 2018, *Nat. Commun.*, 9, 1
- Turner, A. M., Chandra, S., Fortenberry, R. C., & Kaiser, R. I. 2021, *ChemPhysChem*, 22, 985
- Turner, A. M., Koutsogiannis, A. S., Kleimeier, N. F., et al. 2020, *ApJ*, 896, 88
- Tylinski, M., Smith, R. S., & Kay, B. D. 2020, *J. Phys. Chem. C*, 124, 2521
- Tzvetkov, G., Koller, G., Zubavichus, Y., et al. 2004a, *Langmuir*, 20, 10551
- Tzvetkov, G., Ramsey, M., & Netzer, F. 2004b, *Chem. Phys. Lett.*, 397, 392
- Ulbright, H., Zacharia, R., Cindir, N., & Hertel, T. 2006, *Carbon*, 44, 2931
- Van Broekhuizen, F., Pontoppidan, K., Fraser, H., & Van Dishoeck, E. 2005, *A&A*, 441, 249
- Villadsen, T., Ligterink, N. F., & Andersen, M. 2022, *A&A*, 666, A45
- Vinogradoff, V., Duvernay, F., Farabet, M., et al. 2012, *J. Phys. Chem. A*, 116, 2225
- Wang, J., Kleimeier, N. F., Johnson, R. N., et al. 2022a, *PCCP*, 24, 17449
- Wang, J., Marks, J. H., Tuli, L. B., et al. 2022b, *J. Phys. Chem. A*
- Ward, M. D., Hogg, I. A., & Price, S. D. 2012, *MNRAS*, 425, 1264
- Wei, W., Huang, W., & White, J. 2004, *Surf. Sci.*, 572, 401
- Williams, F. J., Bird, D. P., Sykes, E. C. H., Santra, A. K., & Lambert, R. M. 2003, *J. Phys. Chem. B*, 107, 3824
- Xi, M., Yang, M. X., Jo, S. K., Bent, B. E., & Stevens, P. 1994, *J. Chem. Phys.*, 101, 9122
- Yang, Y.-L., Sakai, N., Zhang, Y., et al. 2021, *The Astrophysical Journal*, 910, 20
- Zahidi, E., Castonguay, M., & McBreen, P. 1994, *J. Am. Chem. Soc.*, 116, 5847
- Zhang, Z. E., Yang, Y.-L., Zhang, Y., et al. 2023, *The Astrophysical Journal*, 946, 113
- Zheng, W. & Kaiser, R. I. 2010, *J. Phys. Chem. A*, 114, 5251
- Zhu, C., Frigge, R., Bergantini, A., Fortenberry, R. C., & Kaiser, R. I. 2019a, *ApJ*, 881, 156
- Zhu, C., Frigge, R., Turner, A. M., et al. 2019b, *PCCP*, 21, 1952
- Zhu, C., Frigge, R., Turner, A. M., et al. 2018a, *Chemical Commun.*, 54, 5716
- Zhu, C., Kleimeier, N. F., Turner, A. M., et al. 2022a, *PNAS*, 119, e2111938119
- Zhu, C., Turner, A. M., Abplanalp, M. J., & Kaiser, R. I. 2018b, *ApJS*, 234, 15
- Zhu, C., Wang, H., Medvedkov, I., et al. 2022b, *J. Phys. Chem. Lett.*, 13, 6875

Appendix A: Desorption parameters and molecular constants

The analysis techniques used in this publication make use of a number of molecular constants, such as the moments of inertia, molecule mass, and symmetry factor, which are listed in Table A.1. All the literature studies used in this work and the pre-exponential frequency factors and desorption energies determined with the Redhead-TST method are presented in Table A.2. This table provides an overview of all relevant data to determine the desorption constants (that is, T_{peak} , β), but also information on the desorption surface and how the molecule was produced.

Table A.1. Molecular constants

Molecule	Name	Mass amu	I_x	I_y amu Å^2	I_z	σ
C ₂ H ₄	Ethylene	28	19.08	16.17	2.92	2
CH ₂ NH	Methanimine	29	16.47	14.43	2.04	2
(CH ₂ -O)x	POM	30	14.33	12.86	1.47	2
C ₂ H ₆	Ethane	30	25.17	25.17	6.31	1
N ₂ H ₂	Diazine	30	14.05	13.00	1.05	1
CH ₃ NH ₂	Methylamine	31	22.75	21.84	4.96	1
N ₂ H ₄	Hydrazine	32	20.55	18.71	3.55	1
NH ₂ OH	Hydroxylamine	33	18.70	17.25	2.59	1
CH ₃ CCH	Propyne	40	53.74	53.74	3.17	3
CH ₃ NC	methylisocyanide	41	45.53	45.53	3.17	3
HCCNH ₂	Ethynamine	41	59.06	57.52	1.54	1
c-NCHCH ₂	2H-azirine	41	30.27	19.54	14.32	1
CH ₂ CHCH ₃	Propene	42	58.92	51.88	10.18	1
H ₂ CCO	Ketene	42	48.01	46.54	1.47	2
HCCOH	Ethynol	42	49.29	48.46	0.83	1
CH ₂ CHNH ₂	Vinylamine	43	52.82	44.71	8.15	1
CH ₃ CHNH	Ethanamine	43	52.95	44.79	8.18	1
HNCO	Isocyanic acid	43	45.07	44.48	0.60	1
C ₃ H ₈	Propane	44	68.51	60.81	17.11	1
CH ₂ CHOH	Vinyl alcohol	44	50.29	43.50	6.78	1
CH ₃ CH ₂ NH ₂	Ethylamine	44	64.69	56.89	15.38	1
CH ₃ CHO	Acetaldehyde	44	52.38	46.79	8.74	1
N ₂ O	Nitrous oxide	44	39.93	39.93	0.00	1
[NH ₄ ⁺][CN ⁻]	Ammonium cyanide	44	146.76	146.73	2.83	1
CH ₃ CH ₂ OH	Ethanol	46	63.28	55.54	14.04	1
CH ₃ OCH ₃	Dimethylether	46	52.46	46.86	8.78	1
HCOOH	Formic acid	46	44.30	38.99	5.32	1
NO ₂	Nitrogen dioxide	46	35.88	32.57	3.30	2
HOCH ₂ NH ₂	Aminomethanol	47	60.30	52.63	12.12	1
CH ₃ OOH	Methylhydroperoxide	48	51.92	45.92	10.77	1
CH ₃ PH ₂	methylphosphine	48	34.89	34.54	5.94	1
CH ₃ SH	Methanethiol	48	40.03	38.25	4.95	1
HOCH ₂ OH	Methanediol	48	59.02	51.41	10.77	1
H ₂ POH	Hydroxyphosphine	50	29.81	28.86	3.63	1
HC ₂ CHO	Propynal	54	96.61	88.73	7.88	1
c-H ₂ C ₃ O	Cyclopropenone	54	73.92	58.67	15.25	1
CH ₂ CHCHO	Propenal	56	111.51	102.48	9.03	1
NH ₂ CH ₂ CN	Amino acetonitrile	56	108.85	97.55	15.76	1
c-C ₃ H ₄ O	cyclopropanone	56	82.11	64.18	25.05	1
CH ₃ NCO	Methyl isocyanate	57	107.16	100.76	9.58	1
HOCH ₂ CN	Glycolonitrile	57	108.34	97.44	14.06	1
C ₄ H ₁₀	n-Butane	58	150.85	141.82	21.56	1
CH ₂ CHCH ₂ OH	Allyl alcohol	58	126.85	118.55	16.30	1
CH ₃ CH ₂ CHO	Propanal	58	115.73	112.38	19.84	1
CH ₃ CHCH ₂ O	Propylene oxide	58	86.19	78.08	27.92	1
CH ₃ CHCHOH	1-Propenol	58	108.21	87.30	24.05	1
CH ₃ COCH ₃	Acetone	58	97.26	57.70	45.87	1
CH ₂ CH(OH)CH ₃	2-propenol	59	94.16	52.54	44.76	1
CH ₃ CONH ₂	Acetamide	59	90.84	52.18	41.81	1
CH ₃ NHCHO	N-Methylformamide	59	114.82	107.36	10.60	1
CH ₃ OCH ₂ CH ₃	Ethyl methyl ether	59	136.12	128.10	17.51	1
(CH ₂ NH ₂) ₂	Ethylenediamine	60	143.37	134.37	18.46	1
(CHO) ₂	Glyoxal	60	104.37	96.66	7.71	1
CH ₃ CH ₂ CH ₂ OH	1-Propanol	60	145.92	136.47	18.86	1
CH ₃ COOH	Acetic acid	60	87.60	49.39	41.37	1
CH ₃ OCHO	Methyl formate	60	107.99	102.32	8.84	1
H ₂ CC(OH) ₂	1,1-Ethenediol	60	84.34	45.49	38.85	1
HOCH ₂ CHO	Glycolaldehyde	60	111.18	108.06	16.40	1
HOCHCHOH	1,2-Ethenediol	60	115.96	108.00	7.96	1
NH ₂ CONH ₂	Carbamide	60	84.30	44.12	40.18	2

Table A.1. continued.

Molecule	Name	Mass amu	I_x	I_y amu \AA^2	I_z	σ
OCS	Carbonyl sulfide	60	87.51	87.51	0.00	1
[NH ₄ ⁺][OCN ⁻]	Ammonium cyanate	60	—	—	—	—
c-C ₃ H ₂ O	Cyclopropenone	60	73.92	58.67	15.25	2
NH ₂ CH(CH ₃)OH	alpha-aminoethanol	61	104.80	60.80	56.14	1
NH ₂ COOH	Carbamic acid	61	81.24	41.21	40.04	1
[H ₃ O ⁺][OCN ⁻]	Hydronium cyanate	61	—	—	—	—
(CH ₂ OH) ₂	Ethylene glycole	62	107.48	89.15	33.76	1
CH ₃ OCH ₂ OH	Methoxymethanol	62	132.67	124.49	14.55	1
CH ₃ OOCH ₃	Dimethylperoxide	62	118.60	111.24	13.74	1
CH ₃ SCH ₃	Dimethyl sulphide	62	88.29	66.38	28.27	1
H ₂ CO ₃	Carbonic acid	62	84.91	42.46	42.45	1
HCOPH ₂	Formylphosphine	62	95.53	86.63	8.90	1
HCOSH	Thioformic acid	62	84.10	75.66	8.45	1
[NH ₄ ⁺][HCOO ⁻]	Ammonium formate	63	—	—	—	—
SO ₂	Sulfurdioxide	64	61.48	42.00	0.00	1
H ₂ P(O)OH	Phosphinic acid	66	70.60	54.68	21.39	1
H ₂ S ₂	Hydrogen disulfide	66	73.02	72.66	3.58	1
H ₂ SO ₂	Sulfoxylic acid	66	73.97	51.93	25.33	1
P ₂ H ₄	Diphosphine	66	55.84	55.26	5.62	1
CH ₂ OCHCN	Cyanoethylene oxide	69	141.53	135.73	27.90	1
CH ₃ COCN	Acetyl cyanide	69	150.27	107.53	45.89	1
CHOCH ₂ CN	Cyanoacetaldehyde	69	141.53	135.73	27.90	1
H ₃ SiC(H)CO	Silylketene	72	147.38	138.24	9.14	1
(CH ₃) ₂ NCHO	N-N-Dimethylformamide	73	163.06	115.34	55.81	1
CH ₃ C(O)OCH ₃	Methyl acetate	74	159.72	120.32	46.17	1
CH ₃ CH ₂ OCHO	Ethyl formate	74	213.27	199.56	20.02	1
HCOCOOH	Glyoxylic acid	74	144.61	104.85	39.76	1
[CH ₃ NH ₃ ⁺][NCO ⁻]	Methylammonium cyanate	74	—	—	—	—
HC ₅ N	Cyanobutadiyne	75	328.74	328.74	0.00	1
NH ₂ CH ₂ COOH	Glycine	75	152.20	122.27	50.91	1
CH ₃ CH ₂ CH ₂ SH	n-Propanethiol	76	227.55	216.26	20.70	1
CH ₃ OCOOH	Carbonic acid monomethyl ester	76	150.24	113.70	39.89	1
HOCH ₂ COOH	Glycolic acid	76	153.30	122.07	49.05	1
NCCCCN	Dicyanoacetylene	76	327.44	327.44	0.00	1
[NH ₄ ⁺][CH ₃ COO ⁻]	Ammonium acetate	77	—	—	—	—
C ₆ H ₆	Benzene	78	178.19	89.10	89.09	6
H ₂ PCOOH	Phosphinecarboxylic acid	78	145.75	104.19	44.42	1
[NH ₄ ⁺][NH ₂ COO ⁻]	Ammoniumcarbamate	78	287.19	248.62	49.82	1
CH ₃ P ₂ H ₃	methylidiphosphine	80	144.88	134.69	18.63	1
PH ₂ CH ₂ PH ₂	methyleneidiphosphine	80	144.84	134.66	18.56	1
C ₄ H ₄ S	Thiophene	84	157.93	98.37	59.56	1
c-C ₆ H ₁₂	Cyclohexane	84	201.70	116.67	116.65	1
C ₆ H ₁₄	Hexane	86	473.94	458.27	34.41	1
CH ₃ COCOCH ₃	2,3-Butanedione / diacetyl	86	219.84	148.14	87.40	1
CH ₂ C(OH)COOH	2-Hydroxyacrylic acid	88	209.94	133.12	76.82	1
CH ₃ COCOOH	Pyruvic acid	88	213.52	136.19	80.48	1
HOCH ₂ CH(OH)CHO	Glyceraldehyde	90	285.64	243.94	57.82	1
CH ₃ C ₆ H ₅	Toluene	92	288.03	199.12	92.08	3
HOCH(CH ₂ OH) ₂	Glycerol	92	311.26	269.19	62.35	1
CH ₃ P(O)(OH) ₂	Methylphosphonic acid	96	110.04	108.06	94.31	1
S ₃	Trisulfur	96	187.14	143.31	43.83	2
P ₃ H ₅	Triphosphane	98	154.78	128.94	34.16	1
C ₆ H ₅ CCH	Phenylacetylene	102	401.67	312.32	89.35	2
c-C ₆ H ₅ CN	Benzonitrile	103	401.22	311.94	89.28	2
C ₆ H ₅ CHCH ₂	Styrene	104	412.59	319.77	98.38	1
(CH ₃) ₂ C ₆ H ₄	p-Xylene	106	437.34	348.78	94.87	2
C ₆ H ₅ CHO	Benzaldehyde	106	412.51	316.64	95.87	1
CH ₃ CH ₂ C ₆ H ₅	Ethylbenzene	106	411.55	340.25	112.86	1
C ₄ H ₅ N ₃ O	Cytosine	111	715.27	471.06	244.23	1
C ₈ H ₁₈	Octane	114	1069.05	1046.62	47.45	1

Table A.1. continued.

Molecule	Name	Mass amu	I_x	I_y amu Å^2	I_z	σ
C ₅ H ₆ N ₂ O ₂	Thymine	126	476.79	329.82	150.13	1
C ₁₀ H ₈	Naphthalene	128	571.60	411.14	160.46	2
S ₄	Tetrasulfur	128	371.39	246.23	125.16	2
C ₆ H ₁₅ N ₃	AAT	129	543.23	302.24	299.79	1
C ₅ H ₅ N ₅	Adenine	135	530.47	319.98	210.54	1
C ₁₀ H ₂₂	Decane	142	2046.04	2017.46	59.88	1
CH ₃ I	Methyl iodide	142	66.39	66.39	3.17	3
C ₅ H ₅ N ₅ O	Guanine	151	715.27	471.06	244.23	1
[C ₆ H ₁₅ N ₃ H ⁺][HCOO ⁻]	AATF salt	175	—	—	—	—
C ₁₄ H ₁₀	Phenanthrene	178	1231.44	921.82	309.62	2
C ₂₄ H ₁₂	Coronene	300	3009.29	1504.65	1504.64	6
C ₃₂ H ₁₄	Ovalene	398	5511.77	3406.56	2105.21	2
C ₆₀	Fullerene	720	5214.32	5214.30	5214.24	3

Notes. POM = Polyoxymethylene, AAT = Acetaldehyde Ammonia Trimer, AATF salt = Acetaldehyde Ammonia Trimer Formate salt. For the salts no moments of inertia or symmetry factors have been listed.

Table A.2. Literature and Redhead-TST desorption energies

Molecule ^a	Surface ^b	Precursor(s) ^c	Processing ^d	T_{peak} K	β K s^{-1}	Λ pm	$q_{\text{rot},3D}$	$q_{\text{in},3D}$	ν_{lit} s^{-1}	$E_{\text{des,lit}}$ K	ν_{TST} s^{-1}	$E_{\text{des,Red}}$ K	Reference	
C ₂ H ₄	(P) ASW	C ₂ H ₄	No	68	0.033	40	125	62	4.0E+15	2800	1.1E+16	2780	Behnard et al. (2019)	
C ₂ H ₄	Compact ASW	C ₂ H ₄	No	60	0.033	43	103	55	4.0E+15	2400	7.1E+15	2420	Behnard et al. (2019)	
CH ₂ NH		CH ₃ NH ₂	5 keV e ⁻	115	0.008	30	201	109	-	-	5.3E+16	5110	Zhu et al. (2019b)	
(CH ₂ O)X		H ₂ CO:H ₂ CO	UV	230	0.067	21	426	226	-	-	4.6E+17	10390	Buischer et al. (2016)	
(CH ₂ O)X		H ₂ O:NH ₃ :H ₂ CO	Thermal	225	0.067	21	412	221	-	-	4.3E+17	10140	Duvvunay et al. (2014)	
C ₂ H ₆		CH ₄	UV	66	0.017	39	503	65	-	2060	4.5E+16	2840	Carrasco et al. (2020)	
C ₂ H ₆		C ₂ H ₆	No	67	0.033	39	514	66	6.0E+16	3000	4.7E+16	2840	Behnard et al. (2019)	
C ₂ H ₆	(P) ASW	C ₂ H ₆	No	58	0.033	42	414	57	6.0E+16	2500	2.9E+16	2420	Behnard et al. (2019)	
C ₂ H ₆	Compact ASW	C ₂ H ₆	No	-	1.000	0	0	-	9.5E+15	2490	-	-	Smith et al. (2016)	
C ₂ H ₆	ASW	C ₂ H ₆	No	-	1.000	0	0	-	5.1E+28	2980	-	-	Smith et al. (2016)	
Graphene		C ₂ H ₆	No	75	0.600	37	609	74	-	-	-	-	Tait et al. (2005a)	
MgO(100)		C ₂ H ₆	No	110	0.008	30	237	108	-	-	5.9E+16	3000	Försiel et al. (2017)	
A ^g		CH ₄ :NH ₃	5 keV e ⁻	108	0.008	30	827	110	-	-	2.0E+17	4930	Försiel et al. (2017)	
A ^g		CH ₄ :NH ₃	5 keV e ⁻	148	0.083	26	1326	151	-	-	6.2E+17	6630	Theulé et al. (2011a)	
Cu		CH ₂ NH	H	125	0.083	28	1029	127	-	-	3.4E+17	5510	Theulé et al. (2011a)	
C ₂ H ₆	HOPG	CH ₃ NH ₂	No	160	0.200	25	1490	163	-	7000	8.1E+17	7080	Chaabouni et al. (2018)	
C ₂ H ₆	np-ASW	CH ₃ NH ₂	No	137	0.200	27	1181	139	-	4200	4.7E+17	5970	Chaabouni et al. (2018)	
N ₂ H ₄		CH ₄ :NH ₃	5 keV e ⁻	145	0.008	26	957	152	-	-	4.4E+17	6780	Försiel et al. (2017)	
CH ₃ NH ₂		NO	H	188	0.017	22	1107	204	1.0E+13	6520	8.8E+17	8840	Congiu et al. (2012)	
CH ₃ NH ₂		NO	H	188	0.017	22	1107	204	-	-	8.8E+17	8840	Congiu et al. (2012)	
CH ₃ NH ₂		NO	H	170	0.083	23	952	184	-	-	6.2E+17	7640	Fedosev et al. (2016)	
NH ₂ H ₂		NO:CO	H	200	0.083	21	1214	217	-	-	1.1E+18	9140	Fedosev et al. (2016)	
N ₂ H ₄	(A) Silicate	O		180	1.000	23	1037	195	-	-	7.6E+17	7690	He et al. (2015)	
NH ₂ OH	Rh	NH ₃ :O ₂	5 keV e ⁻	191	0.008	22	1133	207	-	-	9.3E+17	9130	Tsegaw et al. (2017)	
NH ₂ OH		NH ₃ :H ₂ O	5 keV e ⁻	180	0.008	23	1037	195	-	-	7.6E+17	8550	Zheng & Kaiser (2010)	
NH ₂ OH		NO ₂	H	245	0.017	19	1646	265	-	-	2.2E+18	11810	Ioppolo et al. (2014)	
NH ₂ OH		Graphite	H	170	0.083	23	952	184	-	-	4.0E+17	5580	Peck et al. (1998)	
NH ₂ OH		Pt(111)	CH ₃ CCH	138	4.000	23	767	181	-	-	1.5E+17	4690	Turner et al. (2021)	
NH ₂ OH		CH ₃ CCH	5 keV e ⁻	105	0.017	27	509	138	-	-	1.5E+17	4690	Behnard et al. (2019)	
CH ₃ CCH		CH ₃ H ₄	No	97	0.033	28	452	127	1.0E+19	4700	1.2E+17	4230	Behnard et al. (2019)	
CH ₃ CCH		CH ₃ H ₄	No	92	0.033	29	418	121	1.0E+19	4400	9.7E+16	3990	Behnard et al. (2019)	
CH ₃ NC	α -quartz(0001)	CH ₃ NC	No	120	0.200	25	527	161	3.0E+17	4990	2.1E+17	5120	Bertin et al. (2017)	
CH ₃ NC	α -quartz(0001)	CH ₃ NC	No	120	0.200	25	527	161	3.0E+17	5340	2.1E+17	5120	Bertin et al. (2017)	
CH ₃ NC		CH ₃ NC	No	135	0.167	23	629	182	1.0E+18	6270	3.2E+17	5850	Bertin et al. (2017)	
CH ₃ NC		CH ₃ NC	No	135	0.167	23	629	182	1.0E+18	6380	3.2E+17	5850	Bertin et al. (2017)	
CH ₃ NC		CH ₃ NC	No	138	0.167	23	650	186	5.0E+16	5690	3.5E+17	6000	Bertin et al. (2017)	
CH ₃ NC		CH ₃ NC	No	138	0.167	23	650	186	5.0E+16	5690	3.5E+17	6000	Bertin et al. (2017)	
HCCN _{H2}		C ₂ H ₂ :NH ₃	5 keV e ⁻	160	0.017	22	2175	215	-	-	1.6E+18	7590	Turner et al. (2021)	
c-NCH _{H2}		C ₂ H ₂ :NH ₃	5 keV e ⁻	200	0.017	19	3862	269	-	-	4.3E+18	9730	Turner et al. (2021)	
CH ₂ CH ₂ CH ₃	(P) ASW	C ₃ H ₆	No	86	0.033	29	2087	119	6.0E+18	4100	4.4E+17	3860	Behnard et al. (2019)	
CH ₂ CH ₂ CH ₃	Compact ASW	C ₃ H ₆	No	80	0.033	30	1873	110	6.0E+18	3800	3.4E+17	3560	Behnard et al. (2019)	
H ₂ CCO		CO:CH ₄	5 keV e ⁻	93	0.008	28	381	128	-	-	9.5E+16	4160	Maiti et al. (2014a)	
H ₂ CCO		CH ₃ OH	5 keV e ⁻	121	0.008	24	566	167	-	-	2.4E+17	5560	Maiti et al. (2015)	
H ₂ CCO		CH ₃ OH:CO	5 keV e ⁻	123	0.008	24	580	169	-	-	2.5E+17	5660	Maiti et al. (2015)	
H ₂ CCO		H ₂ O:CO	5 keV e ⁻	95	0.017	28	394	131	-	-	1.0E+17	4200	Turner et al. (2020)	
CH ₂ CH ₂ CH ₃		CH ₃ H ₄	UV	170	0.017	21	1460	234	-	-	1.2E+18	8030	Turner et al. (2020)	
CH ₃ CH ₂ :NH ₃		UV		138	0.083	23	3336	195	-	-	1.9E+18	6330	Chuang in prep.	
CH ₃ CH ₂ :NH ₃		UV		138	0.083	23	3351	195	-	-	1.9E+18	6330	Chuang in prep.	
HNCO		HNCO	H	120	0.200	24	676	169	1.0E+28	3960	2.9E+17	5150	Noble et al. (2015)	
HNCO		HOPG	H	120	0.200	24	676	169	1.0E+28	3730	2.9E+17	5150	Noble et al. (2015)	
MgF ₂		CH ₄	UV	84	0.017	29	3050	121	-	-	2.580	6.5E+17	3860	Carrasco et al. (2020)
(P) ASW		C ₃ H ₈	No	73	0.033	31	2471	105	4.0E+18	3500	4.0E+17	3250	Behnard et al. (2019)	
Compact ASW		C ₃ H ₈	No	84	0.033	29	3050	121	4.0E+18	4000	4.0E+17	3800	Behnard et al. (2019)	
ASW		C ₃ H ₈	No	-	1.000	0	0	-	1.1E+16	2840	-	-	Smith et al. (2016)	
Graphene		C ₃ H ₈	No	-	1.000	0	0	-	4.2E+28	3750	-	-	Smith et al. (2016)	
MgO(100)		C ₃ H ₈	No	93	0.600	27	3553	134	4.0E+15	3490	9.2E+17	3980	Tait et al. (2005a)	
C ₃ H ₈		O ₂ :C ₂ H ₂	H	145	0.083	22	3157	209	-	-	2.0E+18	6660	Chuang et al. (2020)	
C ₃ H ₈		CO:CH ₄	5 keV e ⁻	147	0.008	22	3222	212	-	-	2.1E+18	7100	Abplanalp et al. (2016)	
C ₃ H ₈		CO:CH ₄	5 keV e ⁻	147	0.008	22	3222	212	-	-	2.1E+18	7100	Zhu et al. (2022b)	
C ₃ H ₈		CH ₄ :NH ₃	5 keV e ⁻	125	0.008	24	4933	180	-	-	2.3E+18	6030	Försiel et al. (2017)	
CH ₃ CHO		O ₂ :C ₂ H ₂	Au	130	0.083	23	3218	188	-	-	1.6E+18	5930	Chuang et al. (2020)	

Table A2. continued.

Molecule ^a	Surface ^b	Precursor(s) ^c	Processing ^d	T_{peak} K	β K s^{-1}	Λ pm	$q_{\text{rot,3D}}$	$q_{\text{u,3D}}$	η_{H} s^{-1}	$E_{\text{des,lit}}$ K	ν_{TSV} s^{-1}	$E_{\text{des,Red}}$ K	Reference
CH ₃ CHO	Ni	CH ₃ CHO	No	105	1.210	26	2333	151	1.0E+12	2850	7.7E+17	4410	Corazzini et al. (2021)
CH ₃ CHO	Olivine grains	CH ₃ CHO	No	103	1.210	26	2270	149	—	—	7.2E+17	4320	Corazzini et al. (2021)
CH ₃ CHO	Ni	CH ₃ CHO:H ₂ O	No	108	1.210	25	2420	155	1.0E+12	3080	8.4E+17	4530	Corazzini et al. (2021)
CH ₃ CHO	Olivine grains	CH ₃ CHO:H ₂ O	No	108	1.210	25	2444	156	—	—	8.6E+17	4560	Corazzini et al. (2021)
ASW	Ag	CH ₃ CHO	No	100	0.017	26	2171	144	—	4330	—	—	Lasne et al. (2012)
CH ₃ CHO	CO:CH ₄	5 keV e ⁻	H	122	0.008	24	2926	176	—	—	1.3E+18	4610	Zhu et al. (2022b)
N ₂ O	(A) silicate	NO	H	85	0.017	29	0	123	1.0E+13	2770	—	—	Coniglio et al. (2012)
[NH ₄ ⁺]CN ⁻	Au	HCN:NH ₃	Thermal	160	0.083	21	7415	231	—	—	1.6E+17	6970	Danger et al. (2011a)
[NH ₄ ⁺]CN ⁻	Au	HCN:NH ₃ :CH ₂ :NH	Thermal	180	0.083	20	8848	260	—	—	1.6E+17	7860	Danger et al. (2011a)
CH ₃ CHO	CH ₃ OH:CH ₄	5 keV e ⁻	H	147	0.008	21	5875	222	—	—	4.0E+18	7200	Bergantini et al. (2018a)
CH ₃ CHO	CH ₃ CHO:H	CH ₃ CHO	No	160	0.033	20	6671	241	—	—	5.4E+18	7670	Bisschop et al. (2007)
CH ₃ CHO	CH ₃ CHO:H	CH ₃ CHO	No	151	0.500	21	6116	228	—	—	4.4E+18	6790	Burke et al. (2008)
CH ₃ CHO	O ₂ :C ₂ H ₂	H	H	162	0.083	20	6797	244	—	—	5.6E+18	7630	Chuang et al. (2020)
CH ₃ CHO	CH ₃ CHO:H	No	H	169	0.167	20	7242	255	—	—	5.6E+18	7880	Lattelais et al. (2011)
CH ₃ CHO	HOPG	CH ₃ CHO:H	No	162	1.000	20	6797	244	2.0E+15	6010	5.6E+18	7230	Ulbricht et al. (2006)
CH ₃ OC ₃	Ag	CH ₃ OH:CH ₄	5 keV e ⁻	135	0.008	22	3419	204	—	—	2.0E+18	6500	Bergantini et al. (2018a)
CH ₃ OC ₃	(C) H ₂ O	CH ₃ OC ₃	No	—	0.167	0	—	1.0E+14	4080	—	—	—	Lattelais et al. (2011)
HCOOH	Au	HCOOH	No	145	0.200	21	2482	219	—	—	1.6E+18	6510	Chabouin et al. (2020)
HCOOH	Au	CO:O ₂	H	160	0.008	20	2877	241	—	—	2.3E+18	7760	Ioppolo et al. (2011)
NO ₂	(SiO) ₂	NO ₂ +O ₂	O	129	0.083	23	676	195	—	—	3.5E+17	5690	Minissale & Dulieu (2014)
NO ₂	(SiO) ₂	NO ₂ +O ₃	O	122	0.083	23	621	184	—	—	2.9E+17	5350	Minissale & Dulieu (2014)
NO ₂	HOPG	NO ₂	No	144	0.500	21	644	189	—	—	3.2E+17	5500	Minissale & Dulieu (2014)
NO ₂	HOPG	H ₂ O:NH ₃ :H ₂ CO	Thermal	205	0.017	18	8543	316	6.0E+16	4450	5.2E+17	6170	Urbicht et al. (2006)
HOCH ₂ NH ₂	Au	H ₂ O:NH ₃ :HCN	Thermal	214	0.083	17	9112	330	3.0E+12	6980	1.2E+19	10180	Bossa et al. (2009a)
HOCH ₂ NH ₂	Au	HOCH ₂ NH ₂	Thermal	200	0.083	18	8233	308	—	—	1.3E+19	10330	Danger et al. (2012)
HOCH ₂ NH ₂	Ag	CH ₃ NH ₂ :O ₂	5 keV e ⁻	210	0.017	18	8858	324	—	—	1.1E+19	9590	Danger et al. (2012)
CH ₃ OH	Ag	HOCH ₂ O ₂	5 keV e ⁻	162	0.017	20	4903	255	—	—	4.2E+18	10450	Singh et al. (2022)
CH ₃ PH ₂	Ag	CH ₄ :PH ₃	5 keV e ⁻	102	0.017	25	1294	161	—	—	4.2E+18	7850	Zhu et al. (2022a)
CH ₃ SH	Au(111)	CH ₃ SH	No	139	3.000	21	2116	219	1.0E+13	4030	1.3E+18	4660	Turner et al. (2018)
CH ₃ SH	Au(111)	CH ₃ SH	No	160	0.240	20	2614	252	—	—	2.2E+18	7220	Turner et al. (2018)
HOCH ₂ OH	Ag	H ₂ O:NH ₃ :H ₂ CO	Thermal	225	0.067	17	9052	354	—	—	1.5E+18	10940	Duvrenay et al. (2014)
HOCH ₂ OH	Ag	CH ₃ OH:O ₂	5 keV e ⁻	181	0.017	19	6531	285	—	—	7.0E+18	8880	Zhu et al. (2022a)
H ₂ POH	Ag	CO ₂ :PH ₃	5 keV e ⁻	205	0.017	17	2433	336	—	—	3.5E+18	9940	Turner et al. (2018)
H ₂ POH	Ag	H ₂ O:PH ₃	5 keV e ⁻	205	0.017	17	2433	336	—	—	3.5E+18	9940	Turner et al. (2018)
H ₂ POH	Ag	H ₂ O:PH ₃	5 keV e ⁻	177	0.017	19	1952	290	—	—	2.1E+18	8460	Turner et al. (2018)
HC ₂ CHO	Ag	CO:C ₂ H ₂	5 keV e ⁻	140	0.002	20	6387	248	—	—	4.6E+18	7090	Abplanaal & Kaiser (2019)
HC ₂ CHO	Ag	C ₂ H ₂ :CO	5 keV e ⁻	135	0.002	20	6048	239	—	—	4.1E+18	6820	Kleinmeier et al. (2021a)
c-H ₂ C ₃ O	Ag	CO:C ₂ H ₂	5 keV e ⁻	190	0.002	17	9994	337	—	—	1.3E+19	9890	Abplanaal & Kaiser (2019)
c-H ₂ C ₃ O	Ag	c-H ₂ C ₃ O	5 keV e ⁻	180	0.002	18	9216	319	—	—	1.1E+19	9320	Kleinmeier et al. (2021a)
CH ₂ CHCHO	Ag	CO:C ₂ H ₄	5 keV e ⁻	140	0.008	20	7896	257	—	—	5.9E+18	6900	Abplanaal et al. (2015)
CH ₂ CHCHO	Ag	CH ₂ CHCHO	No	164	1.000	18	10011	301	—	—	1.0E+19	7420	Muir et al. (2020)
NH ₂ CH ₂ CN	Ag	HCNN:NH ₃ :NHCH ₂	Thermal	185	0.083	17	15275	340	—	—	2.0E+19	8970	Danger et al. (2011a)
NH ₂ CH ₂ CN	Au	UV	UV	205	0.067	16	17818	377	—	—	2.9E+19	10080	Danger et al. (2011b)
c-H ₂ C ₃ O	Ag	CO:C ₂ H ₄	5 keV e ⁻	110	0.008	22	6220	202	—	—	2.9E+18	5320	Abplanaal et al. (2015)
CH ₃ NCO	Au	CH ₄ :HNCO	UV	145	0.083	19	8334	271	—	—	6.8E+18	6840	Ligterink et al. (2017)
HOCH ₂ CN	Au	CH ₂ CO:NH ₃ :HCN	Thermal	214	0.083	16	17889	400	3.0E+12	6980	3.2E+19	10510	Danger et al. (2012)
HOCH ₂ CN	Au	HCNN:NH ₃ :NHCH ₂	Thermal	208	0.067	16	17151	389	—	—	2.9E+19	10240	Danger et al. (2014)
C ₄ H ₁₀	Ag	Al ₂ O ₃ (0001)	No	—	—	0	—	4.0E+10	4230	—	—	—	Slayton et al. (1995)
C ₄ H ₁₀	Ag	MgO(100)	C ₄ H ₁₀	110	0.600	22	11628	209	5.0E+15	4200	5.6E+18	4920	Tait et al. (2005b)
C ₄ H ₁₀	Ag	MgO(100)	C ₄ H ₁₀	111	0.600	22	11787	211	5.0E+15	4200	5.8E+18	4970	Tait et al. (2005a)
CH ₂ CHCH ₂ OH	Pd(111)	CH ₃ CH ₂ CHO	No	200	0.017	16	20780	381	—	—	6.3E+19	10140	Dostert et al. (2016)
CH ₃ CH ₂ CHO	Ag(111)	CH ₃ CH ₂ CHO	No	162	1.000	18	15542	308	—	—	1.6E+19	7400	Muir et al. (2020)
CH ₃ CH ₂ CHO	Ag	C ₂ H ₂ :CO	5 keV e ⁻	125	0.083	21	10534	238	—	—	6.5E+18	5870	Qasim et al. (2019)
CH ₃ CH ₂ CHO	Ag	CO:CH ₃ CH ₃	5 keV e ⁻	127	0.008	20	10788	242	—	—	6.9E+18	6270	Abplanaal et al. (2016)
CH ₃ CH ₂ CHO	Ag	PCE:E	5 keV e ⁻	120	0.008	21	9908	228	—	—	5.7E+18	5890	Abplanaal et al. (2016)
CH ₃ CH ₂ CHO	Ag	CO ₂ :C ₃ H ₆	5 keV e ⁻	117	0.008	21	8139	223	—	—	4.4E+18	5710	Bergantini et al. (2018b)
CH ₃ CH ₂ CHOH	ASW	CO ₃ CH ₃ CH ₃	5 keV e ⁻	165	0.008	18	14991	314	—	—	1.6E+19	8330	Abplanaal et al. (2016)
CH ₃ COCH ₃	ASW	CH ₃ CO ₂ CH ₃	No	130	0.017	20	11159	247	—	—	7.5E+18	6340	Lasne et al. (2012)
CH ₃ COCH ₃	(C) H ₂ O	CH ₃ COCH ₃	No	140	5.000	19	12471	266	1.0E+13	4210	9.7E+18	6080	Schaff & Roberts (1994)
CH ₃ COCH ₃	ASW	CH ₃ CO ₂ CH ₃	No	157	5.000	18	14811	299	1.0E+13	4810	1.4E+19	6900	Schaff & Roberts (1994)

Table A2. continued.

Molecule ^a	Surface ^b	Precursor(s) ^c	Processing ^d	T_{peak} K	β K s^{-1}	Λ pm	$q_{\text{rot},3D}$	$q_{\text{u},3D}$	η_{u} s^{-1}	$E_{\text{des,lit}}$ K	ν_{337} s^{-1}	$E_{\text{des,Red}}$ K	Reference	
CH ₃ COCH ₃	ASW	CH ₃ COJCH ₃	No	157	4.500	18	14811	299	1.0E+13	4690	1.4E+19	6910	Schaff & Roberts (1998)	
CH ₃ COCH ₃	(P) ASW	CH ₃ C(O)CH ₃	No	145	0.083	19	13145	276	—	—	1.1E+19	6910	Souda (2011)	
CH ₃ COCH ₃	non-(P) ASW	CH ₃ C(O)CH ₃	No	120	0.083	21	9897	228	—	—	5.7E+18	5620	Souda (2011)	
CH ₂ CH(OH)CH ₃	Ag(111)	CH ₂ CH(OH)CH ₃	No	202	1.000	16	20048	391	—	—	3.3E+19	9420	Muir et al. (2020)	
CH ₃ CONH ₂	Au	NH ₂ CH(CH ₃)OH	UV	220	0.067	15	21555	426	—	—	4.2E+19	10920	Duvemay et al. (2010)	
CH ₃ CONH ₂	Au	HNCO:CH ₄	UV	215	0.083	16	20825	416	—	—	3.9E+19	10600	Ligerink et al. (2018a)	
CH ₃ NHCHO	Au	CH ₃ NH ₂ :CO	UV	200	0.067	16	15173	387	—	—	2.4E+19	9800	Bossa et al. (2012)	
CH ₃ NHCHO	Ag	CH ₃ NH ₂ :CO	5keV e ⁻	225	0.008	15	18105	436	—	—	3.7E+19	11610	Frigge et al. (2018b)	
CH ₃ OCH ₂ CH ₃	Ag	H ₂ O:CH ₄	5keV e ⁻	170	0.008	17	18173	329	—	—	2.1E+19	8630	Bergantini et al. (2018c)	
(CH ₂ NH ₂) ₂	Ag	CH ₃ NH ₂	5keV e ⁻	160	0.008	18	17907	315	—	—	1.9E+19	8100	Zhu et al. (2019b)	
(CHO) ₂	Ag	CH ₃ OH:CO	5keV e ⁻	145	0.008	19	7227	285	—	—	6.2E+18	7160	Maiti et al. (2015)	
CH ₃ CH ₂ CH ₂ OH	Ag(111)	CH ₃ CH ₂ CH ₂ OH	No	219	1.000	15	29470	431	—	—	5.8E+19	10350	Muir et al. (2020)	
CH ₃ CH ₂ CH ₂ OH	Au	CH ₃ CH ₂ CHO	H	155	0.083	18	17548	305	—	—	1.7E+19	7470	Qasim et al. (2019)	
CH ₃ COOH	Ag	CH ₄ :CO ₂	5keV e ⁻	165	0.017	18	13035	325	—	—	1.5E+19	8200	Bergantini et al. (2018a)	
CH ₃ COOH	ASW	CH ₃ COOH	No	157	0.017	18	12349	309	1.0E+00	—	1.2E+19	7770	Berlin et al. (2011)	
CH ₃ COOH	HOPG	CH ₃ COOH	No	155	0.500	18	12114	305	—	—	1.2E+19	7130	Burke et al. (2015b)	
CH ₃ COOH	(C) H ₂ O	CH ₃ COOH	No	160	0.500	18	12705	315	—	—	1.3E+19	7390	Burke et al. (2015c)	
CH ₃ COOH	(C) H ₂ O	CH ₃ COOH	No	160	0.017	18	12705	315	—	—	1.3E+19	7930	Lattelais et al. (2011)	
CH ₃ COOH	Ag	CH ₄ :CO ₂	5keV e ⁻	155	0.017	18	12114	305	—	—	1.2E+19	7660	Zhu et al. (2018b)	
CH ₃ OCCHO	ASW	CH ₃ OCCHO	No	128	0.017	20	6717	252	1.0E+14	4450	4.5E+18	6180	Berlin et al. (2011)	
CH ₃ OCCHO	(C) H ₂ O	CH ₃ OCCHO	No	129	0.017	20	6795	254	1.0E+14	4570	4.6E+18	6230	Berlin et al. (2011)	
CH ₃ OCCHO	HOPG	CH ₃ OCCHO	No	104	0.500	22	4919	205	—	—	2.2E+18	4570	Burke et al. (2015b)	
CH ₃ OCCHO	HOPG	CH ₃ OCCHO	No	104	0.500	22	4919	205	—	—	3320	2.2E+18	Burke et al. (2015b)	
CH ₃ OCCHO	HOPG	CH ₃ OCCHO	No	104	0.500	22	4919	205	—	—	3910	2.2E+18	Burke et al. (2015b)	
CH ₃ OCCHO	HOPG	CH ₃ OCCHO	No	104	0.500	22	4919	205	—	—	4140	2.2E+18	Burke et al. (2015b)	
CH ₃ OCCHO	HOPG	CH ₃ OCCHO	No	127	0.500	20	6638	250	—	—	4410	4.4E+18	5690	Burke et al. (2015c)
CH ₃ OCCHO	(C) H ₂ O	CH ₃ OCCHO	No	127	0.500	20	6638	250	—	—	4620	4.4E+18	6440	Zahidi et al. (1994)
CH ₃ OCCHO	(C) H ₂ O	CH ₃ OCCHO	No	127	0.017	20	6638	250	1.0E+14	4480	4.4E+18	6120	Lattelais et al. (2011)	
CH ₃ OCCHO	Ag(111)	CH ₃ OCCHO	No	144	1.500	19	8015	283	—	—	4450	6.8E+18	Schwander et al. (1997)	
CH ₃ OCCHO	Ag(111)	CH ₃ OCCHO	No	160	1.500	18	9387	315	—	—	9.9E+18	7160	Schwander et al. (1997)	
CH ₃ OCCHO	ASW	CH ₃ OCCHO	No	155	2.000	18	8950	305	—	—	8.8E+18	6640	Sexton et al. (1985)	
CH ₃ OCCHO	Mo(111)	CH ₃ OCCHO	No	142	0.500	19	7848	280	—	—	6.5E+18	4970	Sullivan et al. (2016)	
CH ₃ OCCHO	Mo(110)	CH ₃ OCCHO	No	105	0.017	22	4990	207	—	—	2.3E+18	4970	Kleinmeier & Kaiser (2021)	
H ₂ CC(OH) ₂	Ag	CO ₂ :CH ₄	5keV e ⁻	215	0.017	15	18061	423	—	—	3.4E+19	10920	Butscher et al. (2016)	
H ₂ CC(OH) ₂	Ag	CH ₃ OH	5keV e ⁻	210	0.008	16	17435	413	—	—	3.2E+19	10790	Maiti et al. (2015)	
H ₂ CC(OH) ₂	Ag	CH ₃ OH:CO	5keV e ⁻	218	0.008	15	18440	429	—	—	3.6E+19	11240	Maiti et al. (2015)	
HOCH ₂ CHO	Mo(110)	CH ₃ OH	No	145	0.500	19	11502	285	—	—	9.9E+18	6640	Sullivan et al. (2016)	
HOCH ₂ CHO	ASW	HOCH ₂ CHO	No	160	0.500	18	13332	315	—	—	1.4E+19	7390	Burke et al. (2015c)	
HOCH ₂ CHO	(C) H ₂ O	HOCH ₂ CHO	No	160	0.500	18	13332	315	—	—	1.4E+19	7390	Burke et al. (2015c)	
HOCH ₂ CHO	Ag	H ₂ O:CH ₂ CO	UV	200	0.067	16	18632	394	—	—	3.1E+19	9850	Kleinmeier et al. (2021b)	
HOCH ₂ CHO	Ag	CH ₃ OH:CO	5keV e ⁻	166	0.008	17	14089	327	—	—	1.6E+19	8380	Kleinmeier et al. (2021b)	
HOCH ₂ CHO	Ag	CH ₃ OH	1keV e ⁻	145	0.017	19	11502	285	—	—	9.9E+18	7130	Sullivan et al. (2016)	
HOCH ₂ CHO	Ag	CH ₃ OH	5keV e ⁻	210	0.008	16	14261	413	—	—	2.6E+19	10750	Kleinmeier et al. (2021b)	
HOCH ₂ CHO	Ag	CH ₃ OH	5keV e ⁻	225	0.008	15	15816	443	—	—	3.3E+19	11590	Burke et al. (2015c)	
HOCH ₂ CHO	Ag	CH ₃ OH:CO	5keV e ⁻	198	0.008	16	13056	390	—	—	2.1E+19	10080	Kleinmeier et al. (2021b)	
HOCH ₂ CHO	Ag	CH ₃ OH:CO	5keV e ⁻	217	0.008	15	14980	427	—	—	2.9E+19	11140	Kleinmeier et al. (2021b)	
HOCH ₂ CHO	Ag	CH ₃ OH	5keV e ⁻	210	0.008	16	14261	413	1.0E+00	—	2.6E+19	10750	Maiti et al. (2014b)	
HOCH ₂ CHO	Ag	CH ₃ OH	5keV e ⁻	218	0.008	15	15083	429	2.0E+00	—	2.9E+19	11200	Maiti et al. (2014b)	
HOCH ₂ CHO	Ag	CH ₃ OH	5keV e ⁻	250	0.008	14	13337	492	—	—	2.9E+19	12870	Försiel et al. (2016a)	
NH ₂ CONH ₂	Ag	CO:NH ₃	5keV e ⁻	260	0.008	14	12024	512	—	—	3.3E+19	13430	Försiel et al. (2016b)	
NH ₂ CONH ₂	Ag	HNO ₂ :CH ₄	UV	267	0.083	14	12512	526	—	—	3.7E+19	13210	Ligerink et al. (2018a)	
NH ₂ CONH ₂	KBr	H ₂ O:NH ₃ :CO ₂	UV	270	0.033	14	12724	532	—	—	3.8E+19	13620	Popov et al. (2022)	
OCS	HOPG	O	78	0.017	26	0	154	5.3E+14	2430	—	—	—	Ward et al. (2012)	
[NH ₄ ⁺]OCN ⁻	Au	CON ₂	H/N	185	0.083	17	0	364	—	—	2.9E+17	8190	Fedosev et al. (2015b)	
[NH ₄ ⁺]OCN ⁻	Au	NO:CO	UV/H	160	0.083	18	0	315	—	—	2.9E+17	7060	Fedosev et al. (2016)	
[NH ₄ ⁺]OCN ⁻	Au	HNO ₂ :CH ₄	UV	205	0.083	16	0	404	—	—	2.9E+17	9100	Ligerink et al. (2018a)	
c-C ₃ H ₂ O	Ag	CO:C ₂ H ₂	UV	177	0.008	17	4493	348	—	—	5.8E+18	8770	Wang et al. (2022a)	
NH ₂ CH(CH ₃)CHO	Au	NH ₃ :CH ₃ CHO	Thermal	200	0.067	16	25103	400	—	—	4.2E+19	9910	Duvemay et al. (2010)	
NH ₂ COOH	Au	CO ₂ :NH ₃	Thermal	265	0.083	14	23435	530	1.0E+13	9150	6.9E+19	13280	Noble et al. (2014)	
[H ₃ O ⁺]OCN ⁻	Cu	HNO ₂ :H ₂ O	UV	155	0.017	18	0	310	2.9E+12	4810	3.0E+17	7090	Theuls et al. (2011b)	
(CH ₂ OH) ₂	Ag	CH ₃ OH:CH ₄	195	0.008	16	22980	397	—	—	3.7E+19	10040	Bergantini et al. (2018a)		

Table A2. continued.

Molecule ^a	Surface ^b	Precursor(s) ^c	Processing ^d	T_{peak} K	β K s^{-1}	Λ pm	$q_{\text{rel,3D}}$	$q_{\text{rel,3D}}$	η_{ir} s^{-1}	$E_{\text{des,lit}}$ K	v_{TSV} s^{-1}	$E_{\text{des,Ref}}$ K	Reference	
(CH ₂ OH) ₂	Au	H ₂ COH ₂ CO	UV	212	0.067	15	26050	431	-	-	5.0E+19	10550	Butscher et al. (2016)	
(CH ₂ OH) ₂	Au	CO+H ₂ CO	H	200	0.083	16	23870	407	-	-	4.0E+19	9860	Fedosev et al. (2015a)	
(CH ₂ OH) ₂	Au	HOCH ₂ CHO:CO	H	200	0.333	16	23870	407	-	-	4.0E+19	9580	Fedosev et al. (2017)	
(CH ₂ OH) ₂	Rh	HOCH ₂ CHO	H	214	0.017	15	26420	435	-	-	5.1E+19	10960	Leroux et al. (2021)	
(CH ₂ OH) ₂	A _g	5 keV e ⁻	CH ₃ OH	200	0.008	16	23870	407	-	-	4.0E+19	10320	Maiti et al. (2014b)	
(CH ₂ OH) ₂	A _g	5 keV e ⁻	CH ₃ OH:CO	198	0.008	16	23513	403	-	-	3.9E+19	10210	Maiti et al. (2014b)	
(CH ₂ OH) ₂	A _g	5 keV e ⁻	CH ₃ OH	198	0.008	16	23513	403	-	-	3.9E+19	10210	Maiti et al. (2015)	
(CH ₂ OH) ₂	A _g	5 keV e ⁻	CH ₃ OH:CO	198	0.008	16	23513	403	-	-	3.9E+19	10210	Maiti et al. (2015)	
CH ₃ OCH ₂ OH	A _g	5 keV e ⁻	CH ₃ OH:CH ₄	162	0.008	17	15000	330	-	-	1.7E+19	8180	Bergantini et al. (2018a)	
Mo(110)	A _g	20 eV e ⁻	CH ₃ OH	165	0.017	17	15419	336	-	-	1.8E+19	8230	Boamah et al. (2014)	
Mo(110)	A _g	20 eV e ⁻	CH ₃ OH:CH ₄	170	0.008	17	16125	346	-	-	2.0E+19	8620	Bergantini et al. (2015)	
CH ₃ OCH ₂ OH	A _g	5 keV e ⁻	CH ₃ OH:CO	184	0.008	16	18157	374	-	-	2.6E+19	9400	Zhu et al. (2015)	
CH ₃ OCH ₂ OH	A _g	5 keV e ⁻	CH ₃ OH	155	0.017	18	14038	315	-	-	1.4E+19	7690	Schneider et al. (2019)	
CH ₃ OCH ₂ OH	A _g	5 keV e ⁻	CH ₃ OH	161	0.008	17	14861	328	-	-	1.6E+19	8130	Zhu et al. (2019a)	
Mo(110)	A _g	10 eV e ⁻	CH ₃ OH	180	0.017	17	17568	366	-	-	2.4E+19	9050	Sullivan et al. (2016)	
CH ₃ OCH ₃	A _g	5 keV e ⁻	CH ₃ OH:CH ₄	113	0.008	21	7590	230	-	-	4.1E+18	5510	Bergantini et al. (2018a)	
CH ₃ OCH ₃	A _g	5 keV e ⁻	CH ₃ OH	115	0.008	21	7792	234	-	-	4.4E+18	5610	Zhu et al. (2019a)	
CH ₃ SCH ₃	?	Ta(110)	UV	290	0.008	13	29827	590	-	-	1.1E+20	15350	Mahjoub et al. (2017)	
H ₂ CO ₃	A _g	5 keV e ⁻	H ₂ O:CO ₂	245	0.017	14	22261	498	-	-	5.7E+19	12600	Jones et al. (2014)	
H ₂ CO ₃	Al	OH:H ₂ O:CO	OH	235	0.067	14	20912	478	-	-	4.9E+19	11720	Oba et al. (2010)	
H ₂ OPO ₂	A _g	5 keV e ⁻	PH ₃ :CO	125	0.017	20	5629	254	-	-	3.7E+18	6010	Frigge et al. (2018a)	
H ₂ OPO ₂	Rh	CO:H ₂ S	No	131	0.017	19	5157	266	-	-	3.8E+18	6300	Wang et al. (2022b)	
[NH ₄ ⁺]HCOO ⁻	CsI	10 keV e ⁻	H ₂ ₂ S:CH ₃ OH:NH ₃ :H ₂ O	290	0.008	15	0	420	-	-	2.0E+18	9400	Bergner et al. (2016)	
[NH ₄ ⁺]HCOO ⁻	Au	HCOOH:NH ₃	No	208	0.200	15	0	430	7.7E+15	8290	-	2.0E+18	9450	Kruczkiewicz et al. (2021)
SO ₂	A _g	SO ₂	No	142	3.000	18	0	298	-	3920	-	-	-	Liu et al. (2002)
H ₂ PO(OH)	A _g	CO ₂ :PH ₃	H ₂ O:PH ₃	290	0.017	13	21057	628	-	-	8.0E+19	15070	Turner et al. (2018)	
H ₂ PO(OH)	A _g	H ₂ O:PH ₃	H ₂ S	138	0.023	18	3315	299	-	-	2.8E+18	6560	Jimenez-Escobar & Muñoz Caro (2011)	
H ₂ S ₂	?	H ₂ S:H ₂ O	UV	106	0.017	21	5052	230	-	-	2.6E+18	5040	Jimenez-Escobar & Muñoz Caro (2011)	
P ₂ H ₄	A _g	5 keV e ⁻	CH ₄ :PH ₃	130	0.017	19	2897	282	-	-	2.2E+18	6180	Turner et al. (2016)	
CH ₂ OCHCN	HOPG	C ₂ H ₅ CN	O	145	0.017	17	18968	328	-	-	1.9E+19	7220	Kimber et al. (2018)	
CH ₂ OCHCN	HOPG	C ₂ H ₅ CN	O	177	0.017	16	25582	401	-	-	3.8E+19	8980	Tarczay et al. (2017)	
CH ₃ OCN	HOPG	C ₂ H ₅ CN	O	145	0.017	17	22310	328	-	-	2.2E+19	7250	Kimber et al. (2018)	
CH ₃ OCN	HOPG	C ₂ H ₅ CN	O	177	0.017	16	30089	401	-	-	4.4E+19	9000	Kimber et al. (2018)	
CH ₂ OCN	HOPG	C ₂ H ₅ CN	O	145	0.017	17	18968	328	-	-	1.9E+19	7220	Kimber et al. (2018)	
CH ₂ OCN	HOPG	C ₂ H ₅ CN	O	177	0.017	16	25582	401	-	-	3.8E+19	8980	Kimber et al. (2018)	
CH ₃ SiC(H)CO	Rh	SH ₄ :CO	SH ₄ :CO	130	0.008	18	9491	307	-	-	7.9E+18	6440	Tarczay et al. (2017)	
(CH ₃) ₂ NCHO	HOPG	(CH ₃) ₂ NCHO	No	186	1.000	15	38565	445	-	-	2.0E+19	6310	Ulbricht et al. (2006)	
CH ₃ CO(NH ₃) ₂	Ni(111)	CH ₃ CO(NH ₃) ₂	No	165	0.500	16	29623	401	-	-	4.4E+19	7810	Zahidi et al. (1994)	
CH ₃ CO(NH ₃) ₂	HOPG	CH ₃ CO(NH ₃) ₂	No	120	0.500	19	18004	291	4.2E+20	5200	-	4.1E+19	5500	Salter et al. (2018)
CH ₃ CO(NH ₃) ₂	ASW	CH ₃ CO(NH ₃) ₂	No	134	0.500	18	21245	325	1.0E+16	5830	-	1.9E+19	8980	Kimber et al. (2018)
CH ₃ CH ₂ OH	CH ₃ SiC(H)CO	CH ₃ CH ₂ OH	No	116	0.500	19	17111	282	-	-	1.2E+19	5300	Salter et al. (2019)	
Ni(111)	CH ₃ CH ₂ OCO ⁻	CH ₃ CH ₂ OCO ⁻	No	136	0.500	17	21722	330	-	-	2.0E+19	6310	Zahidi et al. (1994)	
CH ₃ CO(NH ₃) ₂	A _g	5 keV e ⁻	H ₂ O:CO	210	0.017	14	35060	510	-	-	7.8E+19	8780	Eckhardt et al. (2006)	
HC ₅ N	A _g	UV	HNC ₅ COH ₄	214	0.083	14	0	520	-	-	6.8E+17	9690	Ligterink et al. (2018a)	
ASW	No	150	0.012	16	0	369	1.0E+13	-	-	-	1.7E+20	-	Coupeaud et al. (2008)	
Al ₂ O ₃	A _g	245	0.083	13	55385	603	-	-	-	3.9E+20	15350	Ioppolo et al. (2021)		
NH ₂ CH ₂ COOH	No	310	1.000	11	7829	763	-	-	-	9.6E+19	10070	Trzvekov et al. (2004a)		
NH ₂ CH ₂ COOH	Au(111)	NH ₂ CH ₂ COOH	No	205	0.240	14	43957	511	-	-	6.6E+19	10150	Rzeznicka et al. (2005)	
CH ₃ COOH	A _g	195	0.008	14	33355	486	-	-	-	1.5E+20	12300	Boamah et al. (2014)		
HOCH ₂ COOH	Mo(110)	CO ₂ :CH ₃ OH	CO ₂ :CH ₃ OH	235	0.017	13	51211	586	-	-	1.7E+20	13160	Marks et al. (2023)	
HOCH ₂ COOH	A _g	247	0.008	13	55184	616	-	-	-	-	-	-	Guenoun et al. (2005)	
NCCCCN	ASW	No	159	0.013	16	0	396	1.0E+13	5050	-	-	-	-	
NCCCCN	Au	No	-	0.013	0	0	-	1.0E+13	6130	-	-	-	-	
[NH ₄ ⁺]CH ₃ COO ⁻	Au	199	0.200	14	503	3.0E+20	9980	-	-	-	1.3E+19	9410	Guenoun et al. (2005)	
C ₆ H ₆	Rh	140	0.008	17	4872	358	-	-	-	5.1E+18	6880	Kruczkiewicz et al. (2021)		
C ₆ H ₆	ASW	141	0.050	17	4924	361	1.0E+13	4690	-	-	5.2E+18	6680	Abphanap et al. (2019)	
C ₆ H ₆	HOPG	148	0.500	16	5296	379	1.0E+13	5470	-	-	6.2E+18	6710	Bahr & Kempf (2007)	
Graphene	C ₆ H ₆	160	1.000	16	5953	409	1.0E+17	6560	-	-	8.1E+18	7200	Smith & Kay (2018)	
Cu(111)	C ₆ H ₆	155	4.000	16	5676	397	-	-	-	-	7.3E+18	6730	Xi et al. (1994)	

Table A.2. continued.

Molecule ^a	Surface ^b	Precursor(s) ^c	Processing ^d	T_{peak} K	β K s ⁻¹	Λ pm	$q_{\text{rot},3D}$	$q_{\text{rot},3D}$	η_{H} s ⁻¹	$E_{\text{des,lit}}$ K	ν_{337} s ⁻¹	$E_{\text{des,Red}}$ K	Reference	
C ₆ H ₆	Cu(111)	C ₆ H ₆	No	195	4.000	14	8009	499	—	—	1.6E+19	8670	Xi et al. (1994)	
C ₆ H ₆	Cu(111)	C ₆ H ₆	No	213	4.000	14	9143	545	—	—	2.2E+19	9560	Xi et al. (1994)	
C ₆ H ₆	Cu(111)	C ₆ H ₆	No	225	4.000	13	9927	576	—	—	2.7E+19	10150	Thrower et al. (2009)	
C ₆ H ₆	(A) silica	C ₆ H ₆	—	0.100	0	0	—	1.0E+13	6250	—	—	—	—	Thrower et al. (2009)
C ₆ H ₆	(A) silica	C ₆ H ₆	—	0.100	0	0	—	1.0E+13	5890	—	—	—	—	Thrower et al. (2009)
C ₆ H ₆	(A) silica	C ₆ H ₆	—	0.100	0	0	—	1.0E+13	5290	—	—	—	—	Thrower et al. (2009)
C ₆ H ₆	(A) silica	C ₆ H ₆	—	0.100	0	0	—	1.0E+13	4990	—	—	—	—	Thrower et al. (2009)
C ₆ H ₆	(A) silica	C ₆ H ₆	No	—	0.100	0	—	1.0E+13	4930	—	—	—	—	Thrower et al. (2009)
C ₆ H ₆	(A) silica	C ₆ H ₆	No	—	0.100	0	—	1.0E+13	4750	—	—	—	—	Ulbricht et al. (2006)
C ₆ H ₆	HOPG	C ₆ H ₆	No	151	0.750	16	5458	386	9.0E+15	5770	6.6E+18	6800	Zhu et al. (2018a)	
C ₆ H ₆	H ₂ PCOOH	PH ₃ :CO ₂	5 keV e ⁻	192	0.017	14	3242	491	—	—	6.4E+19	9850	Noble et al. (2014)	
C ₆ H ₆	[NH ₄ ⁺]NH ₂ COO ⁻	CO ₂ :NH ₃	Thermal	240	0.083	13	104054	614	1.0E+13	8300	6.9E+19	12000	Putapov et al. (2019)	
C ₆ H ₆	(A) carbon	CO ₂ :NH ₃	Thermal	240	0.033	13	104054	614	—	—	6.9E+19	12220	Putapov et al. (2019)	
C ₆ H ₆	MgFeSiO ₄	CO ₂ :NH ₃	Thermal	240	0.033	13	104054	614	—	—	6.9E+19	12220	Putapov et al. (2019)	
C ₆ H ₆	KBr	CO ₂ :NH ₃	Thermal	240	0.033	13	104054	614	—	—	6.9E+19	12220	Putapov et al. (2019)	
C ₆ H ₆	Ag	CH ₄ :PH ₃	5 keV e ⁻	135	0.017	17	14034	354	—	—	1.4E+19	6670	Turner et al. (2016)	
C ₆ H ₆	Ag	CH ₄ :PH ₃	5 keV e ⁻	165	0.017	15	18920	433	—	—	2.8E+19	8310	Turner et al. (2016)	
C ₄ H ₄ S	Au(111)	C ₄ H ₄ S	No	186	3.000	14	36209	513	1.0E+13	5540	7.2E+19	8590	Liu et al. (2002)	
C ₄ H ₄ S	Au(111)	C ₄ H ₄ S	No	142	3.000	16	24153	391	—	—	2.8E+19	6390	Liu et al. (2002)	
c-C ₆ H ₁₂	Graphene	C ₆ H ₆	No	153	1.000	15	46526	422	1.7E+16	6440	6.3E+19	7190	Smith & Kay (2018)	
C ₆ H ₁₄	Al ₂ O ₃ (0001)	C ₆ H ₁₄	No	—	0	0	—	5.4E-09	5230	—	—	—	—	Slayton et al. (1995)
C ₆ H ₁₄	MgO(100)	C ₆ H ₁₄	No	144	0.600	16	70101	406	1.0E+16	5580	8.5E+19	6870	Tait et al. (2005a)	
C ₆ H ₁₄	CH ₂ CH ₂ PH ₂	CH ₃ CHO	5 keV e ⁻	236	0.008	12	90763	666	—	—	3.0E+20	12690	Kleinmeier et al. (2020b)	
C ₆ H ₁₄	CH ₃ COCOCH ₃	CH ₃ COCOCH ₃	No	135	0.008	16	39268	381	—	—	4.2E+19	6920	Kleinmeier et al. (2020b)	
C ₆ H ₁₄	CH ₃ COCOCH ₃	CH ₃ COCOCH ₃	No	158	0.008	15	49719	446	—	—	7.3E+19	8210	Kleinmeier et al. (2020b)	
C ₆ H ₁₄	PA	PA	PA	160	0.008	15	50666	451	—	—	7.6E+19	8320	Kleinmeier et al. (2020b)	
C ₆ H ₁₄	PA	PA	PA	206	0.008	13	74018	581	—	—	1.8E+20	10950	Kleinmeier et al. (2020b)	
C ₆ H ₁₄	PA	PA	PA	236	0.008	12	90763	666	—	—	3.0E+20	12690	Kleinmeier et al. (2020b)	
C ₆ H ₁₄	CH ₃ COCOCH ₃	CH ₃ COCOCH ₃	No	160	0.008	15	50666	451	—	—	7.6E+19	8320	Kleinmeier et al. (2020b)	
C ₆ H ₁₄	CH ₃ COCOCH ₃	CH ₃ COCOCH ₃	No	170	0.008	14	55490	480	—	—	9.4E+19	8890	Kleinmeier et al. (2020b)	
C ₆ H ₁₄	CH ₂ CO(OH)COOH	CH ₃ CHO:CO ₂	5 keV e ⁻	200	0.008	13	61496	577	—	—	1.5E+20	10580	Kleinmeier et al. (2020a)	
C ₆ H ₁₄	CH ₃ COCOOH	CH ₃ COCOOH	5 keV e ⁻	235	0.008	12	81777	679	—	—	2.7E+20	12610	Kleinmeier et al. (2020a)	
C ₆ H ₁₄	CH ₃ COCOOH	CH ₃ COCOOH	No	185	0.008	14	57120	534	—	—	1.2E+20	9730	Kleinmeier et al. (2020a)	
C ₆ H ₁₄	HOCH ₂ CH ₂ CHO:CO	H	215	0.333	13	93892	635	—	—	2.7E+20	10720	Fedosev et al. (2017)		
C ₆ H ₁₄	HOCH ₂ CH ₂ CO	UV	225	0.033	12	100518	664	—	—	3.1E+20	11780	Laysac et al. (2020)		
C ₆ H ₁₄	G	No	230	4.000	12	103887	679	—	—	3.4E+20	10970	McManus et al. (2014)		
C ₆ H ₁₄	G	No	300	4.000	11	154758	886	—	—	8.6E+20	14660	McManus et al. (2014)		
C ₆ H ₁₄	HOPG	CH ₃ C ₆ H ₅	No	149	0.500	15	20673	450	1.0E+13	5650	2.9E+19	6980	Salter et al. (2018)	
CH ₃ C ₆ H ₅	HOPG	CH ₃ C ₆ H ₅	No	179	1.000	14	27221	540	1.0E+19	8180	5.5E+19	8410	Ulbricht et al. (2006)	
CH ₃ C ₆ H ₅	Mo(110)	CH ₃ OH	20 eV e ⁻	280	0.017	11	158901	845	—	—	7.8E+20	15180	Boamah et al. (2014)	
CH ₃ C ₆ H ₅	Au	CH ₃ OH	20 eV e ⁻	240	0.333	12	126098	724	—	—	4.6E+20	12120	Fedosev et al. (2017)	
CH ₃ C ₆ H ₅	Ag	CH ₃ OH	5 keV e ⁻	238	0.008	12	124525	718	—	—	4.4E+20	12890	Kaiser & Maksyutenko (2015)	
CH ₃ C ₆ H ₅	Cu	CH ₃ OH	UV	250	0.033	12	134060	755	—	—	5.3E+20	13250	Laysac et al. (2020)	
CH ₃ C ₆ H ₅	Ag	CH ₃ OH	1 keV e ⁻	234	0.008	12	121399	706	—	—	4.2E+20	12660	Matić et al. (2014b)	
CH ₃ C ₆ H ₅	Mo(110)	CH ₃ OH	1 keV e ⁻	280	0.017	11	158901	845	—	—	7.8E+20	15180	Sullivan et al. (2016)	
CH ₃ C ₆ H ₅	Ag	CH ₃ OH	5 keV e ⁻	250	0.017	11	62113	787	—	—	2.5E+20	13240	Turner et al. (2019)	
S ₃	?	H ₂ S:S:CH ₃ OH:NH ₃ :H ₂ O	10 keV e ⁻	282	0.008	11	38093	888	—	—	2.0E+20	15100	Mahjoub et al. (2017)	
S ₃	P ₃ H ₅	H ₂ S	UV	275	0.023	11	73366	866	—	—	3.6E+20	14600	Jimenez-Escobar & Muñoz Caro (2011)	
S ₃	Ag	CH ₄ :PH ₃	5 keV e ⁻	162	0.017	14	25261	521	—	—	4.4E+19	8230	Turner et al. (2016)	
C ₆ H ₅ CCH	Rh	C ₂ H ₂	5 keV e ⁻	170	0.008	13	55038	569	—	—	1.1E+20	8910	Abplanaip et al. (2019)	
c-C ₆ H ₅ CN	Au(100)	C ₆ H ₅ CN	No	285	4.000	10	119327	963	1.0E+14	9020	6.8E+20	13850	Solomon et al. (1989)	
c-C ₆ H ₅ CN	Cu	C ₆ H ₅ CN	No	155	0.500	13	61397	618	—	—	1.4E+20	9400	Maksyutenko et al. (2022)	
C ₆ H ₅ CHCH ₂	Rh	C ₂ H ₂	5 keV e ⁻	163	0.008	13	11250	556	—	—	2.1E+20	8640	Abplanaip et al. (2019)	
C ₆ H ₅ CHCH ₂	Ag(111)	C ₈ H ₈	No	265	2.000	11	230615	904	1.0E+13	7940	1.2E+21	13180	Wei et al. (2004)	
C ₆ H ₅ CHCH ₂	Ag(100)	C ₈ H ₈	No	330	5.000	9	320471	1126	1.0E+13	5650	5.2E+20	10280	Wei et al. (2004)	
C ₆ H ₅ CHCH ₂	HOPG	(CH ₃) ₂ C ₆ H ₄	No	155	0.500	14	54464	539	3.1E+17	8540	2.5E+21	16440	Williams et al. (2003)	
(CH ₃) ₂ C ₆ H ₄	HOPG	(CH ₃) ₂ C ₆ H ₄	No	153	0.500	14	109806	532	1.0E+16	5990	9.5E+19	7450	Salter et al. (2018)	
C ₆ H ₅ CHO	ASW	C ₆ H ₅ CHO	No	180	0.017	13	126806	626	—	—	4810	3.0E+20	9500	Lasne et al. (2012)
CH ₃ CH ₂ C ₆ H ₅	HOPG	CH ₃ CH ₂ C ₆ H ₅	No	205	1.000	12	173146	713	5.0E+19	9500	5.3E+20	10130	Ulbricht et al. (2006)	
C ₄ H ₅ N ₃ O	Au	Cytosine	No	433	0.250	8	1212828	1577	1.0E+13	14670	1.7E+22	23820	Demers et al. (2002)	

Table A2. continued.

Molecule ^a	Surface ^b	Precursor(s) ^c	Processing ^d	T_{peak} K	β K s ⁻¹	Λ pm	$q_{\text{rot},3D}$	$q_{\text{ir},3D}$	η_{ir} s ⁻¹	$E_{\text{des},\text{lit}}$ K	ν_{TSV} s ⁻¹	$E_{\text{des},\text{red}}$ K	Reference
C ₄ H ₅ N ₂ O	Au(100)	Cyosine	No	428	0.250	8	1191882	1559	—	15400	1.7E+22	23330	Demers et al. (2002)
C ₈ H ₁₈	Al ₂ O ₃ (0001)	C ₈ H ₁₈	No	—	—	0	0	1.6E+12	7350	—	—	—	Slayton et al. (1995)
C ₈ H ₁₈	MgO(100)	C ₈ H ₁₈	No	175	0.600	12	250305	655	7.9E+17	7560	6.0E+20	8730	Tait et al. (2005a)
C ₅ H ₆ N ₂ O ₂	Au	Thymine	No	373	0.250	8	519385	1542	1.0E+13	12510	6.2E+21	20090	Demers et al. (2002)
C ₅ H ₆ N ₂ O ₂	Au(100)	Thymine	No	378	0.250	8	529864	1563	—	13350	6.5E+21	20380	Demers et al. (2002)
C ₁₀ H ₈	Rh	5 keV e ⁻	No	185	0.008	11	114642	777	—	—	3.4E+20	9930	Abplanalp et al. (2019)
C ₁₀ H ₈	HOPG	C ₁₀ H ₈	No	235	1.000	10	164130	987	6.0E+16	9260	7.9E+20	11740	Ulbricht et al. (2006)
S ₄	?	H ₂ S:CH ₃ OH:NH ₃ :H ₂ O	10 keV e ⁻	282	0.008	9	118863	1184	—	—	8.3E+20	15500	Mahjoub et al. (2017)
C ₆ H ₁₅ N ₃	Au	HCOOH:CH ₃ CHNH	Thermal	230	0.067	10	363127	973	—	—	1.7E+21	12280	Vinogradoff et al. (2012)
C ₅ H ₅ N ₅	Au	Adenine	No	448	0.250	7	841125	1984	—	—	1.6E+22	24620	Demers et al. (2002)
C ₅ H ₅ N ₅	Au	Adenine binding site 1	No	363	0.250	8	613484	1608	1.0E+13	12150	7.5E+21	19600	Östblom et al. (2005)
C ₅ H ₅ N ₅	Au	Adenine binding site 2	No	443	0.250	7	827083	1962	1.0E+13	14910	1.5E+22	24320	Östblom et al. (2005)
C ₅ H ₅ N ₅	Au	Adenine binding site 3	No	483	0.250	7	941595	2139	1.0E+13	16360	2.0E+22	26710	Östblom et al. (2005)
C ₁₀ H ₂₂	MgO(100)	C ₁₀ H ₂₂	No	204	0.600	10	679726	950	1.3E+19	9370	2.7E+21	10520	Tait et al. (2005a)
CH ₃ I	ASW	CH ₃ I	No	115	3.000	14	721	536	—	—	9.3E+17	4760	DeSimone et al. (2013)
CH ₃ I	(P) ASW	CH ₃ I	No	115	3.000	14	721	536	—	—	9.3E+17	4760	DeSimone et al. (2013)
C ₅ H ₅ N ₅ O	Au(100)	Guanine	No	488	0.250	6	1451100	2418	—	17560	3.6E+22	27260	Demers et al. (2002)
C ₅ H ₅ N ₅ O	Au	Guanine	No	453	0.250	7	1297821	2244	1.0E+13	15280	2.7E+22	25160	Östblom et al. (2005)
[C ₆ H ₅ N ₃ H ⁺] ⁺ [HCOO ⁻]	Au	HCOOH:CH ₃ CHNH	Thermal	270	0.067	8	0	1550	—	—	—	14460	Vinogradoff et al. (2012)
[C ₆ H ₅ N ₃ H ⁺] ⁺ [HCOO ⁻]	Au	HCOOH:C ₆ H ₅ N ₃	Thermal	260	0.067	8	0	1493	—	—	—	13910	Vinogradoff et al. (2012)
C ₁₄ H ₁₀	Rh	5 keV e ⁻	No	232	0.008	9	491510	1355	—	—	3.2E+21	13020	Abplanalp et al. (2019)
C ₂₄ H ₁₂	HOPG	C ₂₄ H ₁₂	No	390	2.000	5	1572181	3839	2.0E+16	15280	4.9E+22	21010	Ulbricht et al. (2006)
C ₃₂ H ₁₄	HOPG	C ₃₂ H ₁₄	No	490	2.000	4	15999447	6399	5.0E+21	27660	1.0E+24	28010	Ulbricht et al. (2006)
C ₆₀	HOPG	C ₆₀	No	573	2.000	3	25544230	13536	2.0E+13	19600	4.1E+24	33630	Ulbricht et al. (2006)

Notes. ^aPOM = Polyoxymethylene, AAT = Acetaldehyde Trimer, AATF salt = Acetaldehyde Ammonia Trimer Formate salt. ^b(P) = porous, (C) = crystalline. ^cP:C:E = CH₃CH₂CHO:CO:CH₃CH₂CHO:CO:CH₃CH₂CHO. G = HOCH₂CH(OH)CHO. ^dH = Hydrogenation, O = Oxygenation

Appendix B: Elemental ratios

Based on the desorption parameters found in this work and assumed abundances, the ice elemental composition is determined throughout a protoplanetary disk, see Sect. 4.4. The radial variations in elemental ratios are presented in Fig. B.1. Figure B.2 presents the [Phosphorus]/[Carbon] ratio plotted against temperature.

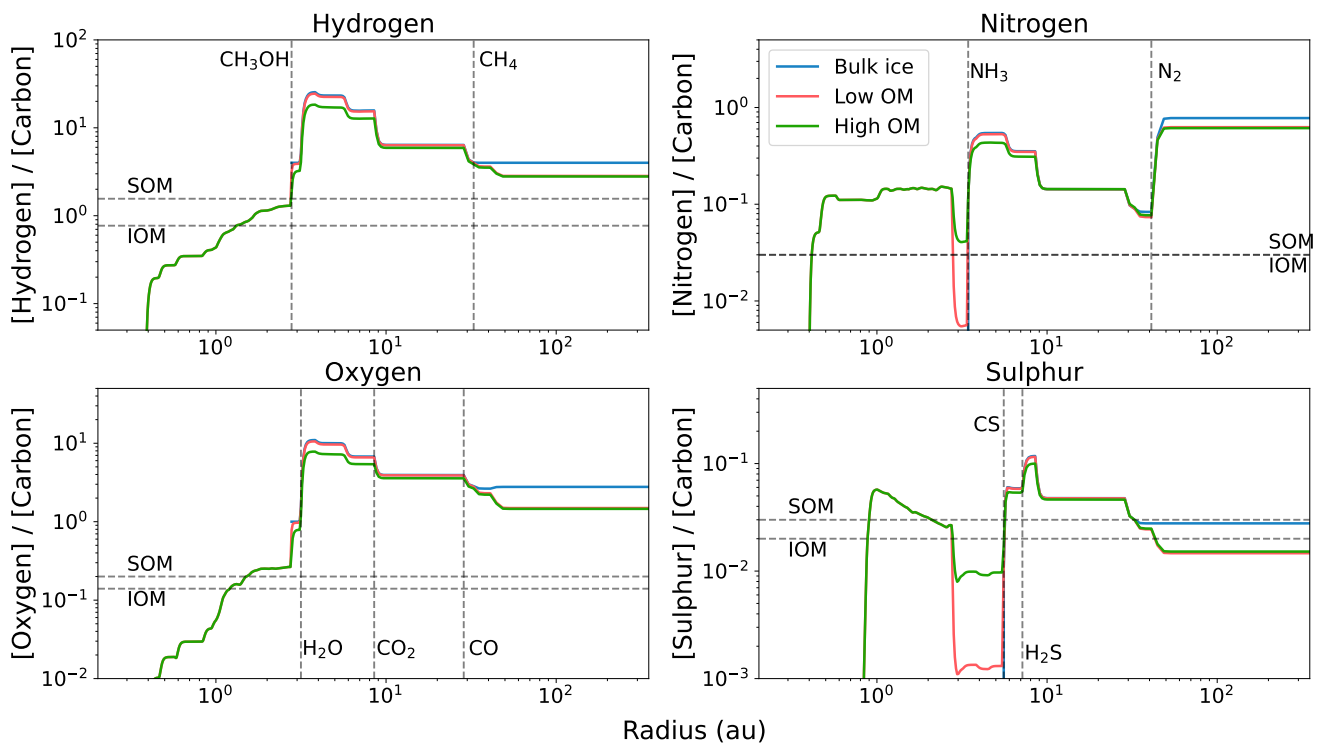


Fig. B.1. Ice elemental composition as $[X]/[\text{Carbon}]$ for Hydrogen, Nitrogen, Oxygen, and Sulphur as a function of protoplanetary disk radius. Peak desorption radii for selected species are indicated in the plot (vertical dashed lines). Elemental compositions of Soluble Organic Matter (SOM) obtained from the Murchison meteorite (Schmitt-Kopplin et al. 2010) and averaged Insoluble Organic Matter (IOM) (Alexander et al. 2017) are indicated (horizontal dashed lines). The desorption profiles are simulated with a first-order Polanyi-Wigner equation, variable surface coverages, and a heating rate of 1 K century^{-1} . An average protoplanetary disk temperature profile of $T(r) = 200 \times (r/1\text{AU})^{0.62}$ (Andrews & Williams 2007) is used to determine the radii.

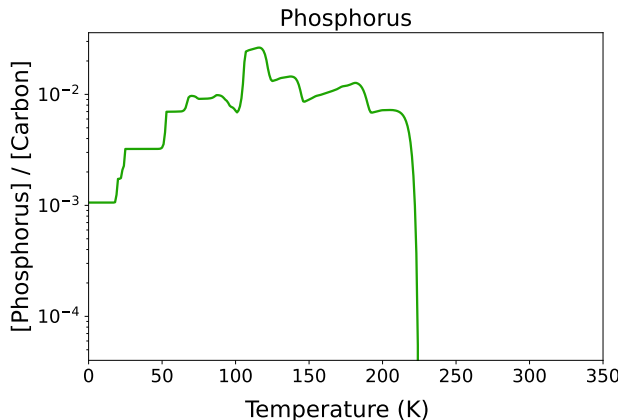


Fig. B.2. Ice elemental composition $[\text{Phosphorus}]/[\text{Carbon}]$ as a function of temperature. The desorption profiles are simulated with a first-order Polanyi-Wigner equation, variable surface coverages, and a heating rate of 1 K century^{-1} .